GSA DATA REPOSITORY 2014273

Two modes for dune orientation - Supplementary information

Sylvain Courrech du Pont,[1,*] Clément Narteau,[2] and Xin Gao[2]

[1] *Laboratoire Matière et Systèmes Complexes, Sorbonne Paris Cité, Université Paris-Diderot, CNRS UMR 7057, 10 rue Alice Domon et Lonie Duquet, 75205 Paris Cedex 13, France*
[2] *Institut de Physique du Globe de Paris, Sorbonne Paris Cité, Université Paris Diderot, CNRS UMR 7154, 1 rue Jussieu, 75238 Paris Cedex 05, France*

Contents

I. MODEL FOR A BIDIRECTIONAL WIND REGIME

We identify two different growth modes for dunes. When dunes develop on an erodible ground, they grow in height and wavelength with sediment coming from the inter dune. This is the recognized scenario of the bed instability. When dunes develop on a non-erodible floor from a localized sediment source, they extend away from the source in the sediment transport direction. We call this new mode of growth (and orientation) the fingering mode. In the following, we derive a simple model for dune orientation from the physical mechanisms implied by these two modes of growth. First, we write the equation for the sand flux over a dune, including a first order perturbation by the dune topography. We then derive the equations for dune orientation when considering an idealized bimodal wind regime. In such a regime, orientations have analytical solutions and we can compare and discuss the orientations and the growth rates attached to the two modes.

A. Sand flux over a linear dune

Let us consider two winds $\vec{W}_1$ and $\vec{W}_N$ of equal strength but with different directions and time durations, alternatively blowing on a linear dune of width W and height H as shown on figure 1. In the standard basis $(\vec{i},\vec{j})$, $\vec{W}_N$ is pointing in the $\vec{i}$ direction, while $\vec{W}_1$ is making an angle θ with $\vec{W}_N$ and $\vec{i}$. Within a full period, $\vec{W}_N$ blows on the

*Electronic address: sylvain.courrech@univ-paris-diderot.fr

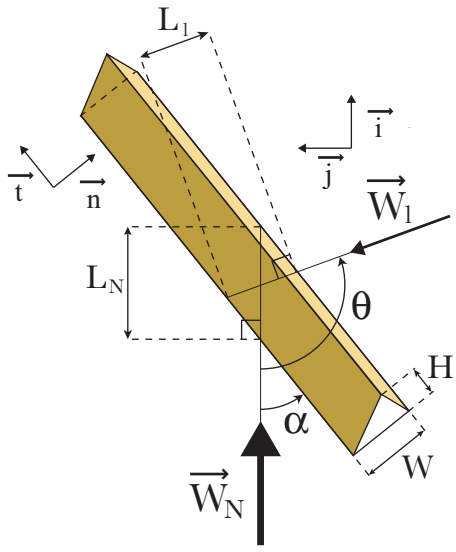

FIG. 1: Sketch of a linear dune submitted to a bimodal wind regime.

dune N times longer than $\vec{W}_1$. The dune trend is making an angle α with $\vec{W}_N$ (and $\vec{i}$), the normal and tangential unit vectors attached to the dune are $\vec{n} = \sin\alpha\,\vec{i} - \cos\alpha\,\vec{j}$ and $\vec{t} = \cos\alpha\,\vec{i} + \sin\alpha\,\vec{j}$.
A positive topography makes the wind accelerate so that the sand flux over a dune depends on the dune shape. For 2D turbulent flows over low hills, Jackson & Hunt show analytically that the speed-up factor, *i.e* the wind velocity increase at the top of the hill, is approximately proportional to the hump aspect ratio [1]. In the present case, the actual magnitude of sand fluxes depends on the angles the dune is making with the winds. To the first order in the dune aspect ratio H/W, the maximum value of the saturated flux $\vec{Q}_{sN}$ associated to the wind $\vec{W}_N$ is:

$$\vec{Q}_{sN} = Q_0\left(1+\beta\frac{H}{L_N}\right)\vec{i} = Q_0\left(1+\beta\frac{H}{W}|\sin\alpha|\right)\vec{i}, \tag{1}$$

where Q_0 is the value of the saturated sand flux over a flat sand bed and β a dimensionless coefficient that accounts for the wind speed-up. Similarly, the maximum value of the saturated flux $\vec{Q}_{s1}$ associated to the wind $\vec{W}_1$ is:

$$\vec{Q}_{s1} = Q_0\left(1+\beta\frac{H}{L_1}\right)\left(\cos\theta\vec{i}+\sin\theta\vec{j}\right) = Q_0\left[1+\beta\frac{H}{W}|\sin(\theta-\alpha)|\right]\left(\cos\theta\vec{i}+\sin\theta\vec{j}\right). \tag{2}$$

The interaction between the sediment transport and the dune shape makes the direction of the mean sand flux, averaged over a full period, depend on the dune orientation. Considering this effect to the first order with a constant aspect ratio H/W over time, it reads:

$$\left\langle\vec{Q}_s\right\rangle = \frac{1}{N+1}\left(N\vec{Q}_{sN}+\vec{Q}_{s1}\right) = \frac{Q_0}{N+1}\{[N\,(1+\gamma|\sin\alpha|)+\cos\theta\,(1+\gamma|\sin(\theta-\alpha)|)]\;\vec{i}+\sin\theta\,(1+\gamma|\sin(\theta-\alpha)|)\,\vec{j}\,\}, \tag{3}$$

where $\gamma = \beta H/W$.

B. Bed Instability

The law of mass conservation in 2 dimensions is $\partial Q/\partial x = -\partial h/\partial t$ where the sand flux Q and the bed-form height h are functions of space x (in the direction of the sand flux) and time t. If the structure is not advected, then $(1/h)\partial h/\partial t$ is the growth rate of the structure. When the structure displays an avalanche face downwind, or more generally when the boundary layer detaches at the dune crest, the sediment flux over the dune typically varies from its maximum saturated value to zero on a characteristic length that scales with the dune length in the wind direction, *i.e* L_1 and L_N for $\vec{W}_1$ and $\vec{W}_N$ respectively (see fig. 1). Then, assuming a constant dune shape (H and W), the growth rate σ averaged over a full period scales like:

$$\sigma \propto \frac{1}{H(N+1)}\left(\frac{Q_{s1}}{L_1}+N\frac{Q_{sN}}{L_N}\right) = \frac{Q_0}{(N+1)HW}\left[|\sin(\theta-\alpha)|+\gamma\sin^2(\theta-\alpha)+N|\sin\alpha|+N\gamma\sin^2\alpha\right]. \tag{4}$$

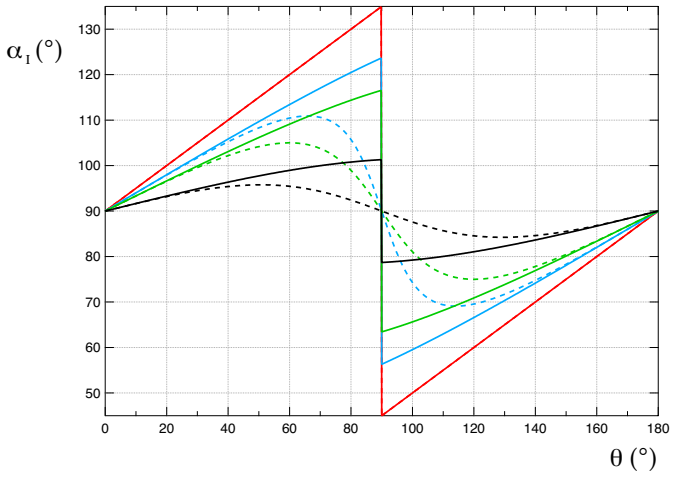

FIG. 2: Dune orientation α_I with respect to the main wind $\vec{W}_N$ in the bed instability mode as a function of the angle θ between the two winds. α_I is calculated with eq. 5 ($\gamma = 0$, full lines) and eq. 6 ($\gamma = +\infty$, dotted lines) for different time duration ratios N between winds (red: $N = 1$, blue: $N = 1.5$, green: $N = 2$ and black: $N = 5$).

σ is a function of the dune orientation α. If the dune is big enough to integrate the multidirectional wind regime, the actual orientation that should emerge is the one with the highest growth rate, such that $d\sigma/d\alpha = 0$. As defined, the resulting dune orientation α_I maximizes the sediment flux perpendicular to the dune crest [2] [53]. If one considers a constant aspect ratio overtime (and so a constant γ value), then, depending on the value of the coefficient γ, α_I ranges between:

$$\begin{cases} \tan\alpha_I = -\dfrac{N+\cos\theta}{\sin\theta}, & \text{for } \theta < \pi/2 \\ \tan\alpha_I = \dfrac{N-\cos\theta}{\sin\theta}, & \text{for } \theta \geqslant \pi/2 \end{cases}, \text{ when } \gamma = 0, \tag{5}$$

which is the solution when considering the flow not disturbed, and:

$$\tan(2\alpha_I) = \frac{\sin(2\theta)}{\cos(2\theta)+N}, \text{ when } \gamma = +\infty, \tag{6}$$

which is the solution when only considering the flow perturbation due to the dune. The solution 5 was already proposed by Rubin and Hunter [2] and is known as the maximum gross bedform-normal transport concept (MGBNT).

The dune orientation α_I in the bed instability mode, solution of equations 5 and 6, is plot as a function of the angle between the two winds θ on figure 2 for several transport ratio N values. When the angle θ between the two winds is smaller than $\pi/2$, the two winds blow towards the same side of the dune. For a given angle θ between the two winds, α_I decreases with N from $\pi/2 + \theta/2$ when $N = 1$ to $\pi/2$ when $N = +\infty$. When the angle θ between the two winds is bigger than $\pi/2$, the two winds blow on either side of the dune. Then, for a given angle θ, α_I increases with N from $\theta/2$ when $N = 1$ to $\pi/2$ when $N = +\infty$. One sees that the effect of the dune aspect ratio on the sediment flux results in a dune trend that is even more perpendicular to the main wind $\vec{W}_N$, especially for θ values around $\pi/2$ and wind time duration ratio N slightly bigger than 1. Equation 6 (for $\gamma = +\infty$) is also the orientation that is found in the limit of large wave length λ, when extending to a bimodal wind regime, the linear stability analysis for transverse dunes done in [3]. Indeed, when the dune profile is smooth, the boundary layer does not detach at the top of the dune, so that the sediment flux typically varies from its maximum saturated value to the undisturbed one (Q_0, the one on a flat sand bed), over the dune length. Moreover, height does not come into play for incipient dunes so that σ scales like $1/\lambda^2$. Finally, note that in the bed instability orientation, the sediment flux $\left\langle \vec{Q}_s \right\rangle$ (eq. 3) has components in the normal and in the tangential directions to the dune crest when θ is bigger than $\pi/2$ (figs. 5 B, 7A).

On another hand, when the instability is mainly growing by pattern coarsening controlled by the advection of dunes, one can expect dunes to be perpendicular to the sediment flux. Although we did not observe such an orientation in

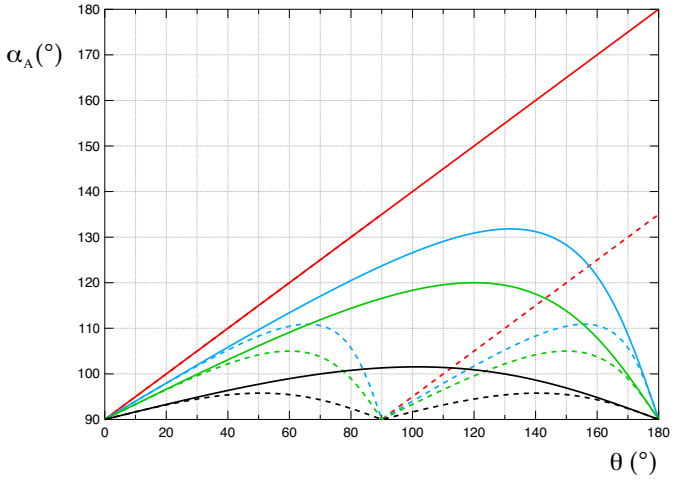

FIG. 3: Dune orientation α_A in the advection mode as a function of the angle θ between the two winds. α_A is calculated with eq. 8 ($\gamma = 0$, full lines) and eq. 9 ($\gamma = +\infty$, dotted lines) for different time duration ratios N between winds (red: $N = 1$, blue: $N = 1.5$, green: $N = 2$ and black: $N = 5$).

experiments, it is interesting to develop this hypothesis. The sediment flux in the direction of the dune orientation would be null, *i.e* $\left\langle \vec{Q}_s \right\rangle . \vec{t} = 0$, and the dune orientation α_A solution of:

$$N \cos\alpha_A \left(1 + \gamma |\sin\alpha_A|\right) + \cos(\theta - \alpha_A) \left[1 + \gamma |\sin(\theta - \alpha_A)|\right] = 0. \tag{7}$$

Depending on γ value, the dune orientation would then range between:

$$\tan\alpha_A = -\frac{N + \cos\theta}{\sin\theta}, \text{ when } \gamma = 0, \tag{8}$$

and

$$\begin{cases} \tan(2\alpha_A) = \dfrac{\sin(2\theta)}{N + \cos(2\theta)}, \text{ for } \theta < \pi/2 \\ \tan(2\alpha_A) = \dfrac{\sin(2\theta)}{\cos(2\theta) - N}, \text{ for } \theta \geqslant \pi/2 \end{cases}, \tag{9}$$

when $\gamma = +\infty$.

The dune orientation α_A in the coarsening-advection mode, solution of equations 8 and 9, is plot as a function of the angle θ between the two winds on figure 3. When θ is smaller than $\pi/2$, the orientation α_A is the same as α_I ; but the two orientations differ when θ is bigger than $\pi/2$. Then, for a given θ value, α_A decreases with N from $\theta/2 + \pi/2$ (resp. $\theta/2 + \pi/4$ when $\gamma = 0$ (resp. $\gamma = +\infty$ and $N = 1$ to $\pi/2$ for $N = +\infty$. This orientation has not been observed experimentally for linear dunes.

C. Dune fingering

When a dune forms from a localized sediment source thanks to two alternate winds that make an angle θ bigger than $\pi/2$, we experimentally observe an elongating finger. If the source is fixed, the structure should align with the mean flux (eq. 3) and make an angle α_F with the main wind $\vec{W}_N$, such that:

$$\tan\alpha_F = \frac{\sin\theta \left[1 + \gamma \sin(\theta - \alpha_F)\right]}{N \left(1 + \gamma \sin\alpha_F\right) + \cos\theta \left[1 + \gamma \sin(\theta - \alpha_F)\right]}. \tag{10}$$

Depending on the γ value, the dune orientation α_F ranges from:

$$\tan\alpha_F = \frac{\sin\theta}{N + \cos\theta}, \text{ when } \gamma = 0 \text{ to :} \tag{11}$$

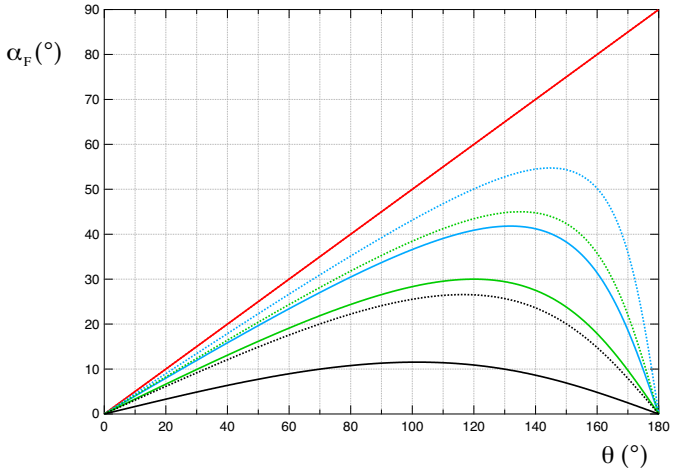

FIG. 4: Dune orientation α_F, *i.e* the angle between the dune trend and the main wind, in the fingering mode as a function of the angle θ between the two winds. α_F is calculated with eq. 11 ($\gamma = 0$, full lines) and eq. 12 ($\gamma = +\infty$, dotted lines) for different time duration ratios N between winds (red: $N = 1$, blue: $N = 1.5$, green: $N = 2$ and black: $N = 5$).

$$\tan \alpha_F = \frac{\sin \theta}{\sqrt{N} + \cos \theta}, \text{ when } \gamma = +\infty. \tag{12}$$

The dune orientation α_F in the fingering mode, solution of equations 11 and 12, is plot as a function of the angle θ between the two winds on figure 4. For a given θ, α_F decreases with N, from $\theta/2$ when $N = 1$ to 0 when $N = +\infty$. The effect of the dune aspect ratio on the sediment flux inhibits the alignment of the dune in the main wind $\vec{W}_N$ direction. The second wind $\vec{W}_1$ blows the dune more perpendicularly to the crest, experiences a bigger aspect ratio and consequently transports more sand. Note that this modification of the overall sediment transport by the dune aspect ratio and orientation is all the more important if the ratio between the resultant drift potential and the drift potential (RDP/DP) is small. It then explains the coexistence of multiple crest orientations and in particular the direction of extension of star dunes arms, when the overall zero order sand flux is null [4].

D. Wind speed-up

A bump makes the wind accelerate: the wind velocity is bigger at the top of the hill than at the toe. Jackson & Hunt have calculated an analytical solution for the 2D turbulent flow over a symmetric smooth profile [1]. They describe the increase in velocity with a fractional speed-up ratio, which is, for a given position along and above the hump profile, the increase in velocity divided by the undisturbed velocity (*i.e* far from the hill). The actual magnitude of the fractional speed-up ratio depends on the hump shape and roughness but, close to the surface, it is proportional to the hump aspect ratio. They find it to be bigger for turbulent flows than for potential flows, and to reach its maximum close (but upwind) to the top of the hill. Many laboratory and field studies report measurement of this fractional speed-up ratio [5–16]. For low dunes or dunes with an aspect ratio typical to transverse dunes, when measured close to the surface in the turbulent boundary layer, they report a maximum value (close to the dune brink) ranging between 0.4 and 1. If we assume that the sediment flux scales as the square of the wind velocity [17], it corresponds to γ ($\gamma = \beta H/L$) values ranging between 0.8 and 2 (between 1.2 and 3 if the flux scales as the cube of the velocity) [54]. In our experiments, finger dunes have a bigger aspect ratio than the ones growing from a sand bed. Moreover, Walker & Nickling have measured a slightly bigger fractional speed-up ratio for an isolated dune than for closely spaced transverse dunes [13]. Not to mention that the fractional speed-up ratio may be a function of time (for a reversing dune, for example), it may significantly vary from one dune to the other and is expected to be bigger for finger dunes than for dunes in the bed instability mode. Nevertheless, we expect these variations of the fractional speed-up ratio, to be small compared to its modulation when changing the angle between the dune and the incident wind. We take $\gamma = 1$ for the discussion that follows and for the field studies.

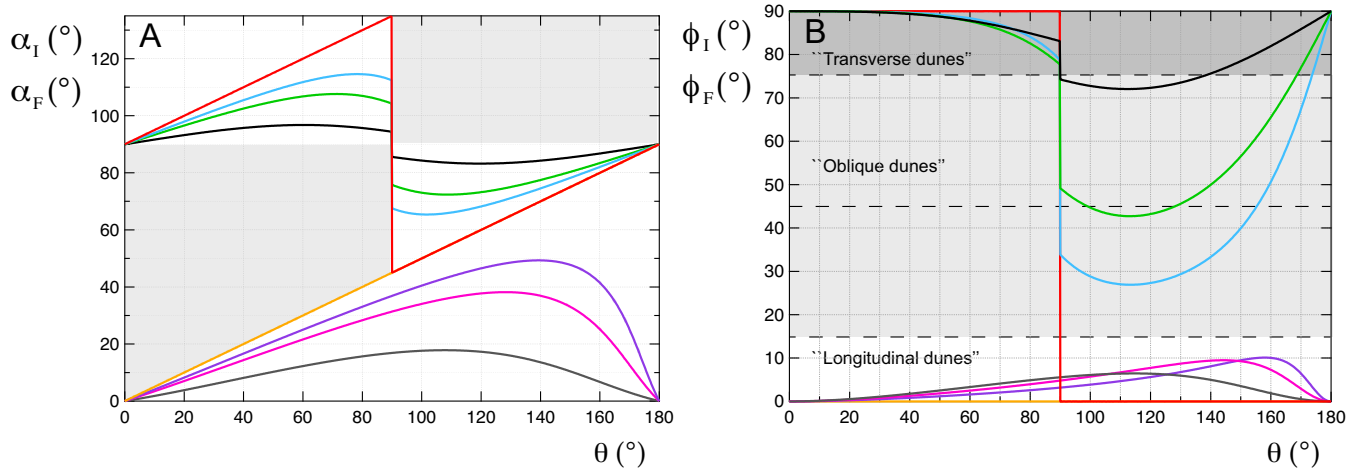

FIG. 5: Orientation of dunes in the two modes. A) Orientation α_I and α_F of dune trends with respect to the prevailing wind in the two modes as a function of the divergence angle θ between winds. α_I curves stand above the line $\theta/2$ while α_F curves stand below this line. No dunes are expected in grey areas of the diagram. B) Orientation Φ_I and Φ_F of dune trends with respect to the resultant (mean flux direction on a flat ground) in the two modes as a function of the divergence angle θ between winds. Dunes whose orientation stands above (resp. under) the 45° line are rather perpendicular (resp. parallel) to the resultant. Grey areas delimitate dune orientation ranges upon the "classical" denomination for dunes regarding their orientation with the resultant [18]. Dunes in the bed instability mode can be transverse, oblique or longitudinal. Finger dunes can only be longitudinal or oblique. Here $\gamma = 1$ for all calculations. Colours represent different time duration ratios N between winds. For the bed instability mode: red: $N = 1$, blue: $N = 1.5$, green: $N = 2$ and black: $N = 5$. For the fingering mode: orange: $N = 1$, pink: $N = 1.5$, violet: $N = 2$ and grey: $N = 5$.

E. Discussion

Figure 5A compares α_I and α_F for $\gamma = 1$. When the angle θ between the two winds is smaller than $\pi/2$, dunes in the bed instability mode grow perpendicular to the mean sand flux direction. The angle α_I between the dune trend and the prevailing wind is equal to $\pi/2 + \theta/2$ when $N = 1$ and tends to $\pi/2$ when N increases. The "speed-up" emphasizes the influence of the prevailing wind. The orientation α_F of dunes in the fingering mode is almost perpendicular to dunes in the bed instability mode ($\alpha_I - \alpha_F$ is exactly $\pi/2$ if $\gamma = 0$). When $N = 1$, $\alpha_F = \theta/2$ and α_F decreases (dunes tend to align with the prevailing wind) when N increases. The speed-up weakens this trend.

When the two winds make an angle θ bigger than $\pi/2$ and have the same time duration ($N = 1$), the resulting orientation of dunes is the same for the bed instability mode and the dune fingering mode. Dunes make an angle $\theta/2$ with the two winds, *i.e* they are aligned with the bisector of the angle between the two wind directions. Increasing the time ratio N shifts the dune orientation, which tends to be perpendicular to the prevailing wind in the bed instability mode and parallel to it in the fingering mode. The two orientations move away from each other when N increases, on each side of the bisector. Taking into account the effect of the aspect ratio, the flux associated to a given wind increases as the wind blows more perpendicular to the dune. As a result, it reinforces the prevalence of the prevailing wind in the bed instability mode but weakens it in the fingering mode. When N increases, the dune orientation tends more rapidly to be perpendicular to the prevailing wind in the bed instability mode than to be parallel to it in the fingering mode.

The same dune orientations with respect to the transport resultant, ϕ_I and ϕ_F, are plotted in figure 5B. The resultant orientation, which is the orientation of the mean sand flux over a flat bed (but not the one over a topography as we have seen), is the one usually reported as the resultant drift potential (RDP) direction. Hunter *et al.* defined dunes regarding their orientation with the resultant direction [18]. Dunes are transverse when this orientation is between 85° and 90°, longitudinal between 0° and 15° and oblique between 15° and 85°. One sees that finger dunes are always oriented more or less parallel to the mean wind ($\phi_F < 45°$) and correspond to dunes which are usually defined as longitudinal or oblique dunes. In our model, α_F is actually always smaller than 20°, so that most of dunes in the fingering mode are longitudinal. However, dunes in the bed instability mode can have orientation ϕ_I bigger but also smaller than 45°. They can cover the whole range (from 0° to 90°) and to that respect can correspond to dunes usually defined as transverse, oblique or longitudinal dunes. Thus, the morphogenesis of dunes is not set when

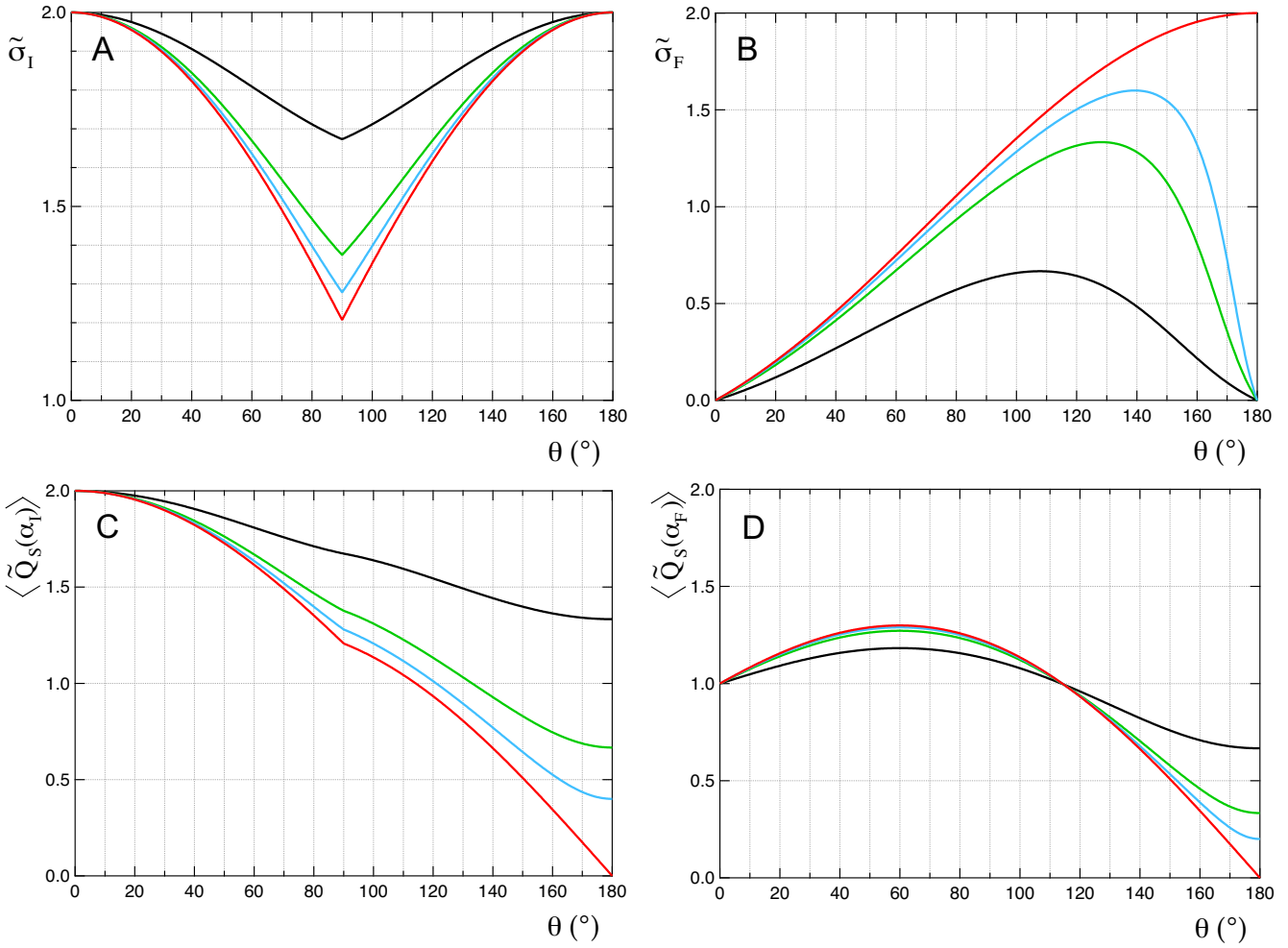

FIG. 6: Comparison of growth rates and fluxes in bed instability and fingering modes. A) Dimensionless growth rate $\tilde{\sigma}_I$ of structures in the bed instability mode as a function of the angle θ between the two winds. B)"Dimensionless growth rate" $\tilde{\sigma}_F$ of structures in the fingering mode as a function of the angle θ between the two winds. $\tilde{\sigma}_I$ and $\tilde{\sigma}_F$ are calculated with equation 4. Equation 4 is non-dimensionalized and normalised by $Q_0/(HW)$. C) Magnitude of the dimensionless mean saturated flux $\left\langle \tilde{Q}_s(\alpha_I) \right\rangle$ in the bed instability mode as a function of θ. D) Magnitude of the dimensionless mean saturated flux $\left\langle \tilde{Q}_s(\alpha_F) \right\rangle$ in the fingering mode as a function of θ. Mean saturated fluxes (eq. 3) are nondimensionalized and normalised by Q_0. $\gamma = 1$ in all calculations where α value is α_I or α_F, whether we consider the bed instabilility or the fingering mode. In all figures, colours represent different time ratios N (red: $N = 1$, blue: $N = 1.5$, green: $N = 2$ and black: $N = 5$).

defining dunes using their orientation with the RDP, or using the criteria of tangential flux or lateral migration. Figure 7B shows the difference between the two orientations α_I and α_F as a function of the angle θ between winds.

We now briefly discuss the conditions and the parameter ranges where patterns in one mode or the other are likely to be observed by comparing fluxes, growth rates and characteristic angles in both modes. Figure 6 displays the"growth rates" $\widetilde{\sigma}_I$ (a) and $\widetilde{\sigma}_F$ (b) and the mean saturated fluxes $< \widetilde{Q}_s(\alpha_I) >$ (c) and $< \widetilde{Q}_s(\alpha_F) >$ (d) corresponding to dunes orientated in each mode as a function of the angle θ between the two winds and for different time ratios N between winds. By definition, $\widetilde{\sigma}_I$ is always bigger than $\widetilde{\sigma}_F$, so that the bed instability mode should be observed when dunes grow and develop from a sand bed with no restriction in sand availability or in a region where there is a net deposition, *i.e.* with a negative divergence of sediment flux. When the divergent angle θ is bigger than $\pi/2$, the flux direction is oblique to the orientation of dunes in the bed instability mode (fig. 7A). Obviously, these dunes shift sideways. On another hand, if patterns develop on a nonerodible floor from localized sand sources, either barchans or finger dunes should be observed.

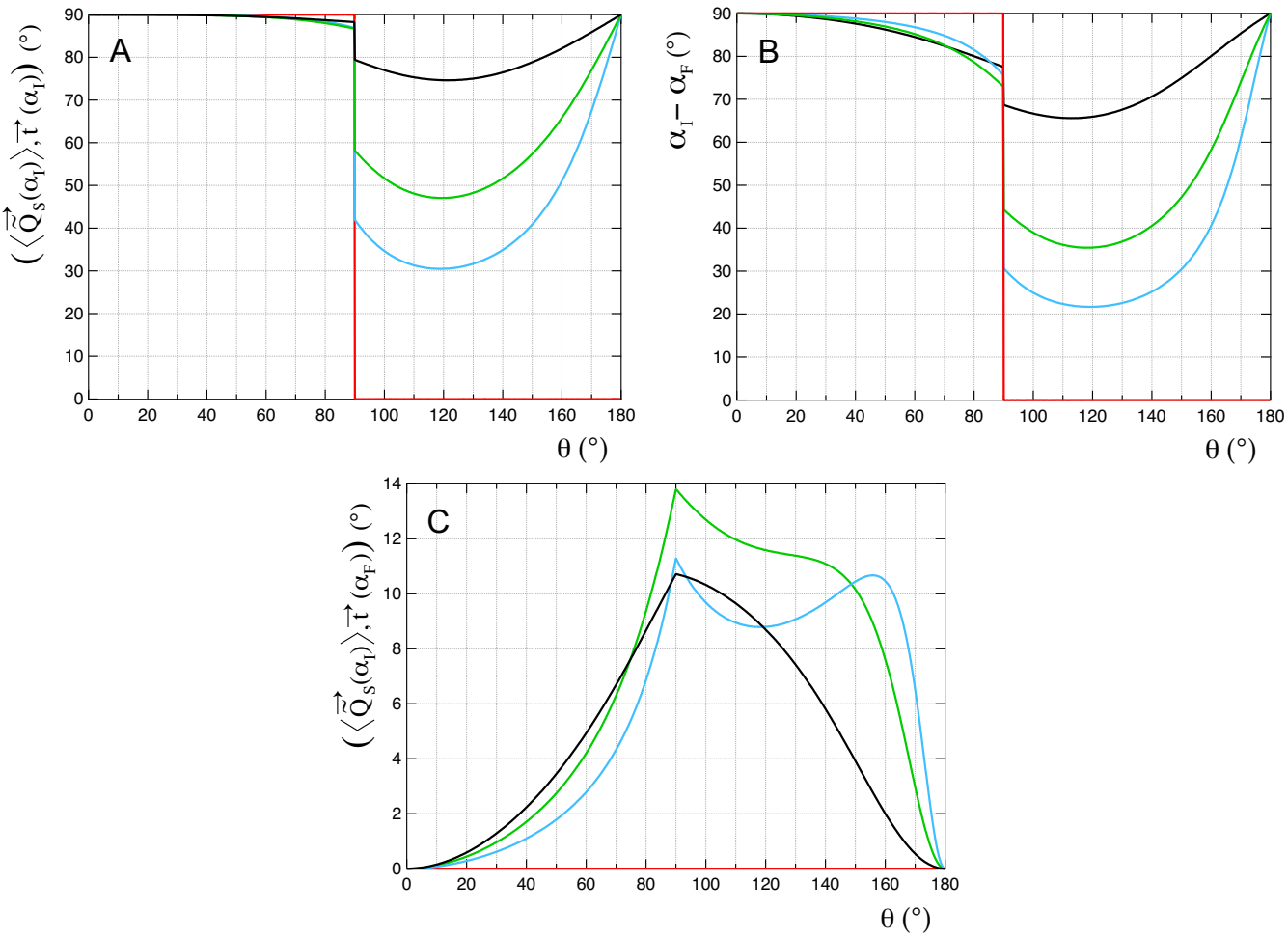

FIG. 7: A) Angle between the dune orientation and the mean saturated flux in the bed instability mode as a function of θ. B) Difference $\alpha_I - \alpha_F$ between dune orientations in the bed instability and the fingering modes as a function of θ. C) Angle between the dune orientation in the fingering mode and the mean saturated flux in the bed instability mode as a function of θ. $\gamma = 1$ in all calculations and α value is α_I or α_F, whether we consider the bed instabilility or the fingering mode. In all figures, colours stand for time ratios N (red: $N = 1$, blue: $N = 1.5$, green: $N = 2$ and black: $N = 5$).

With no global influx, fingers elongate in time but do not grow in height. Although finger dunes elongate and propagate in the direction of the mean sediment flux, without increasing in height, a consistent "growth rate" (erosion at the toe and deposition at the brink) is essential for the very existence of the dune. Otherwise, a crest cannot develop and a substantial aspect ratio cannot be sustained. In a bidirectional wind regime, the finger dune pointing in the mean flux direction is blown on either side by winds. As shown on figure 6 B, these winds can provide a significant "growth rate" that obviously builds and sustains a substantial aspect ratio for the dune.

Finger dunes represent an erodible floor where the bed instability mode can develop as a superimposed pattern. The bed instability is a convective instability, so that dunes migrate as they are growing. The velocity and the direction of advection of dunes in the bed instability mode with respect to the finger dune orientation, as growth rate of both modes, determine the stability of a finger dune. The flux direction in the bed instability mode, *i.e.* the direction of propagation of dunes, can significantly differ from the finger dune orientation (fig. 7 C). As a result, superimposed dunes in the bed instability mode may not have time to fully develop and break the finger dune before they eventually fall down the lee side of the finger dune. Note that the "speed-up effect" may here be of prime importance as the angle between the finger dune and the flux direction for the bed instability is zero if the effect of the aspect ratio is not taken into account (*i.e.* if $\gamma = 0$). This may explain why finger dunes elongate and do not have a limited extension like the horns of barchans. For this latter, because of their symmetry in regards with flux direction, the bed instability can fully develop on their arms and prevent their extension (as shown on figure 6B the "growth rate" $\widetilde{\sigma}_F$ also falls to zero for barchans).

One observes that $\widetilde{\sigma}_F$ is vanishing when θ goes to 0° or 180° and when N is increasing (fig. 6B). Fingering dunes are thus unlikely for small θ, big θ and for big N values. In this range of parameters (to determine), a localized source of sediment should rather emit a row of barchanoid dunes.

In the parameter range where both modes can occur, the observation of one mode or the other should mainly depend on sand availability through the initial and the limit conditions. The bed instability mode should be observed if dunes develop with no restriction in sand availability, while the fingering mode should be observed if dunes develop on a nonerodible floor from localized sand sources. These are ideal cases but the two modes may partially share their range of stability. One can easily imagine that finger dunes remain stable with a global incoming sand flux. The two modes of orientation may also co-exist. The bed instability mode can develop as a superimposed pattern on a finger dune. On their side, dunes in the bed instability mode are advected (migrate perpendicularly to their crest) and thus, are wavy with defects that could align or join in the fingering mode. In our experiments, this is what dramatically happens to dunes growing from a flat bed with a limited depth of sand, once the nonerodible floor appears. Like transverse dunes, dunes in the bed instability mode are unstable and break into barchanoids without sand supply. Each of these barchanoids are (advecting) sources for the development of finger dunes.

Here, the two modes of orientation are discussed using a very simple model. We restrict the sand flow to its minimum ingredients, avoiding the use of free parameters. For example, in our analysis, the growth rate is directly proportional to the divergence of the sediment flux, neglecting that part of the flux propagates the structure. We also neglect secondary flows, which lead to deflection of the sediment flux, or tip effect [9, 12, 15, 19–23]. These secondary flows are likely to significantly affect the dune orientation for big divergent angles where the flux value due to the primary flow is small (fig. 6D). The speed-up is simply taken proportional to the dune aspect ratio, which is considered constant over time, when winds reverse the dune crest. In addition, dunes are considered without defects and isolated, not being part of an interacting dune field. On the field, the sediment sources of finger dunes may also propagate. Despite these simplifications, we expect this analysis to capture the essential phenomena and to give the right picture of the underlying physical mechanisms. There are two modes for the orientation of dunes: the bed instability mode, which selects the orientation of dunes with the higher growth rate, and the fingering mode, in which dunes elongate in the direction of the sediment flux. This analysis can easily be extended to multimodal and complex wind regimes.

II. EXPERIMENTS

In this section we describe our experimental approach (dunes under water) and methods. Then, we compare the results to our model predictions.

A. Dunes underwater

A flat sand bed, when submitted to a unidirectional flow strong enough to transport grains, destabilizes into transverse dunes. For aeolian dunes, the first observed wavelength is about 20 meters long. This finite value of the most unstable wavelength is to be compared to the minimum dune size observed in barchans fields. When smaller than a few meters long, a barchan loses its avalanche face (turns into a dome), quickly erodes and vanishes. A bumpy bedform is unstable and grows in height if the top of bumps is a place where sediment is deposited, *i.e.* where the sediment flux decreases. A bump accelerates the wind velocity and, for a turbulent flow, the maximum value of the shear velocity is reached before the top of the hill [1]. However, because of inertia, the wind needs a characteristic distance to charge in grains. The sediment flux adapts to a change in wind velocity, and reaches its saturated value on a characteristic distance called the saturation length l_s. If the dune is smaller than a few l_s, the top of the dune is eroded, the dune flattens. On the contrary, if it is longer than the minimum size set by l_s, the top of the hill is a place where the sediment flux decreases and the dune grows in height [3]. The saturation length scales as the drag length, *i.e.* the characteristic distance at the end of which a grain initially at rest, reaches the fluid velocity. For a turbulent flow l_s scales like $l_s \propto d\,\rho_s/\rho_f$, where d is the grain diameter, ρ_s the grain density and ρ_f the transporting fluid density [24, 25]. Water being 800 times denser than air, dunes are downscaled by a factor 800 in water and bedforms destabilize at a centimeter scale [26]. Moreover, the characteristic timescales and velocities depend on dune size and are downscaled accordingly.

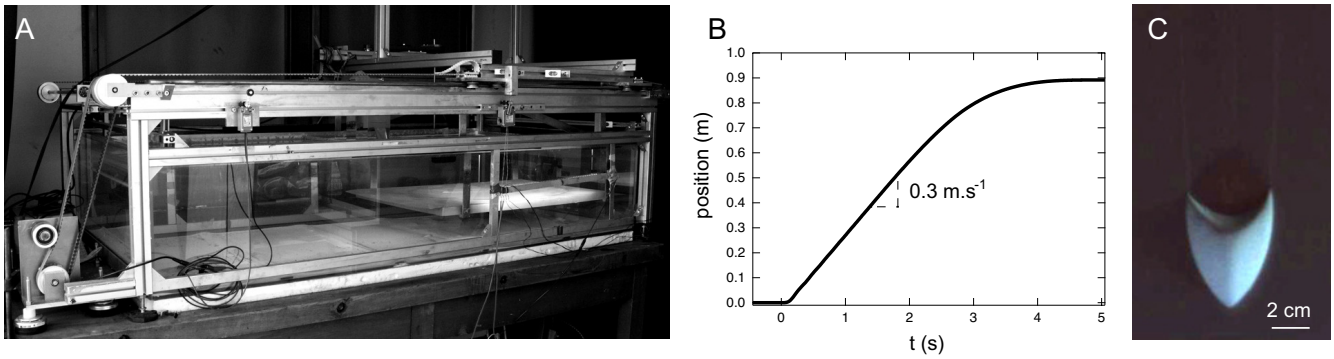

FIG. 8: A: Experimental setup. B: Quick motion of the plate. C: Centimetric barchan underwater (the flow is going from bottom to top).

B. Experimental setup

Our experimental setup is a plate (90 cm wide and 1 m long) that is moved under water in a 2 m long tank (fig.8A). The flow is generated by the translation of the plate from one end to the other of the water tank (fig. 8B). It accelerates to a maximum velocity of 30 cm.s^{-1}, gently stops and goes back to its initial position at a much slower velocity ($\sim$ 2 cm.s^{-1}). In the frame of the moving plate, this asymmetric unidirectional translation motion simulates a unidirectional flow for grains and dunes that lie on the plate. The grains, ceramic beads of volumic mass $\rho_s \simeq 3800$ kg.m^{-3} and diameter $d \simeq 90$ μm, only move during the quick motion of the plate. The return velocity is slower than the threshold transport. When repeated, this elementary motion (a blow) quickly shapes a conical pile of a few grams into a centimetric barchan that migrates on the plate (fig. 8C). The center of the plate is a 70 cm diameter disc that can rotate to change the flow direction relative to the sand bed. This rotation is slow enough to prevent grain motion. This approach was successfully used to study the formation and dynamics of barchans with a unidirectional flow [25] and of transverse and longitudinal dunes in a periodic symmetric bimodal flow regime [26].

In this study, bedforms and dunes are submitted to asymmetric bidirectional flow regimes. Between two alternate plate rotations of an angle θ ($-\theta$), we keep constant the number of blows in one direction (2 blows) and change the number $N \times 2$ of blows in the prevailing flow direction. Thus, a full period counts $2N + 2$ blows. We perform experiments with N equals 1, 2 or 5 and θ equals 100, 130 or 150°. Additionally we vary the initial conditions and the sand supply. To that respect, we perform 3 kinds of experiments:

- starting from a flat sand bed of 1.5 kg of ceramic beads spread over the rotating plate ($\sim$ 1.7 mm high) without further sand supply,
- starting from a flat sand bed of 1.5 kg with sand supply, *i.e.* adding sediment where the bottom plate is visible every 3 or 4 periods.
- starting from a localized conical pile of 1 g and periodically adding sand at the same location point (typically 0.3-0.4 g every 18 or 24 blows).

The morphology of the sand bed is followed through time, which is measured in numbers of blows, thanks to a CCD camera that takes top-view images and a scanner that acquires 3D profiles. These profiles are 12 cm large and as long as the sand bed with a resolution of 120 μm in the horizontal plane and 10 μm in height.

C. Orientation, amplitude and wavelength measurements

Orientation, amplitude and wavelength of dunes are measured with the 3D profiles. During an experiment, 3D profiles are acquired at each plate rotation, after the 2 blows of the subdominant flow and after the $N \times 2$ blows of the prevailing flow. Figure 9B shows a 3D profile of the dune field after the 2 blows of the subdominant flow at time $t = 662$ blows (110 periods) for a full sand supply experiment with $\theta = 128°$ and $N = 2$. Dunes height is taken to be two standard deviations of the dune height profile. The orientation of dunes is defined as the direction giving the higher auto-correlation (fig. 9C). The wavelength is then two times the distance between the maximum and the first minimum of the auto-correlation, in the direction perpendicular to the orientation of dunes. In practice, we calculate

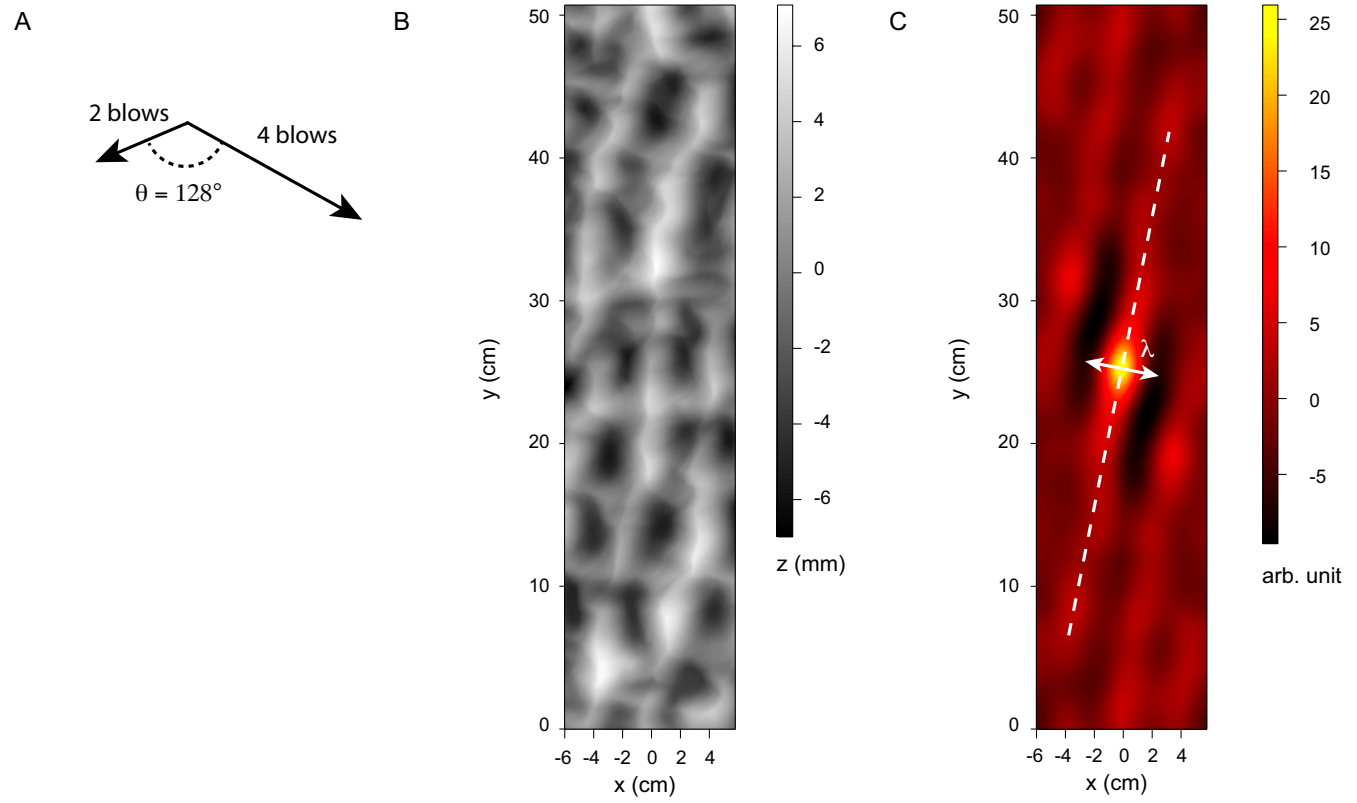

FIG. 9: A: Flow regime: $\theta = 128°$ and $N = 2$. The two vectors show the two directions of the flow for the scan (fig. B) and auto-correlation (fig. C) pictures orientation. B: Scan of the dune field after the 2 blows of the subdominant flow at time $t = 662$ blows (110 periods) for a full sand supply experiment ($\theta = 128°$ and $N = 2$). The standard deviation of the height profile is 2.4 mm. C: Auto-correlation of the height profile (fig. B). The dashed line shows the dune orientation (the direction of maximum auto-correlation). The wavelength λ is the distance between the two first minima of the auto-correlation in a direction perpendicular to the dune orientation. Here dunes have an orientation of 72.2° with the prevailing flow direction. The wavelength is 52.2 mm.

for each direction (every 0.1°) the sum of the auto-correlation value along segments of starting point the center of the auto-correlation and of length 2, 3 or 4 times the wavelength. The direction giving the maximum value for the sum is the orientation of dunes. The orientation of dunes and the wavelength depend on each other. Thus, the orientation of dunes is first calculated with a fixed arbitrary segment length. The calculation is then made several times so that orientation and wavelength values converge. The orientation of dunes is averaged over the different values obtained for the different segment length and between orientations found after the 2 blows of the subdominant flow and the $N \times 2$ blows of the prevailing flow.
The orientation of finger dunes is measured the same way but from the auto-correlation of pictures.

D. Finger dunes growing from a sand bar

Figure 10 shows dunes growing from a transverse sand bar (without further sand supply) with $\theta = 130°$ and $N = 5$. The initial sand bar is perpendicular to the prevailing flow direction. Without sand supply, the transverse dune is unstable and breaks [26]. Instead of breaking into barchans, which happens with a mono-directional flow [26–28], the transverse dune turns into an array of extending finger dunes. This was already observed by Reffet *et al.* for a symmetric bimodal flow regime [26]. Within the same flow regime, the observed array of finger dunes shows the same orientation than an isolated finger dune growing from a localized sand source (fig. 10).

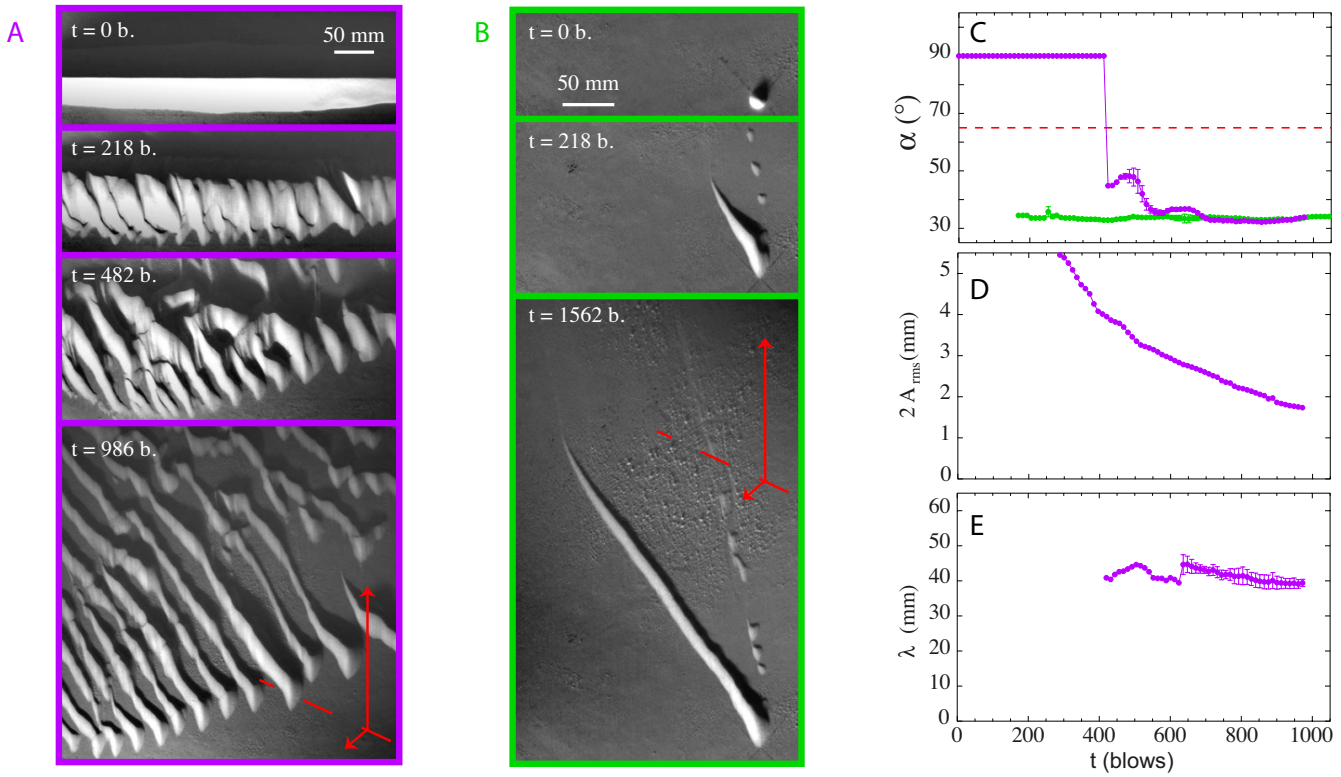

FIG. 10: Comparison of finger dunes growing from the destabilization of a transverse dune or from a localized sand source. The flow regime is characterized by $\theta = 130°$ and $N = 5$. A: Snapshots of a transverse dune breaking into an array of finger dunes. B: Snapshots of a finger dune growing from a localized sand source. The flow regime is the same as in figure A. Arrows show the two flow directions and relative transport potentials. The dashed line is the bisector of the angle between the two flow directions. C: Orientation α of dunes with the prevailing flow direction as a function of time t. D: Amplitude of dunes as a function of time. E: Wavelength of dunes as a function of time. The wavelength is measured once the transverse bar has broken. The (final) breaking wavelength is controlled by the dune height. Violet: Dunes growing from a transverse sand bar. Green: Dune growing from a point source.

E. Orientation of dunes in experiments

Figure 11 compares the orientation of dunes in the experiment to the model prediction (equations 5, 6, 11 and 12).

Experimental orientations of dunes in the bed instability mode are well predicted and stand between the prediction curves of eq. 5 with $\gamma = 0$ (*i.e.* neglecting the "speed-up" effect) and eq. 6 with $\gamma = \infty$ (*i.e.* with the "speed-up" effect only). Data points lie closer to the curves of eq. 6 with $\gamma = \infty$, which suggests a high "speed-up" effect. The "speed-up" correction is all the more important as the divergence angle θ is closer to 90°, to accurately predict dune orientations in the bed instability mode.

However, the model underestimates the angle of finger dunes with the prevailing flow direction: dunes in the model are more aligned with the prevailing flow direction than they are in experiments. This suggests an underestimation of the "speed-up" effect and the possible need of higher order terms in the model. In the model, the sediment flow is also restricted to the direction of the "undeflected" fluid flow. It does not consider secondary flows like the deflection of flux in the lee side [9, 12, 15, 19, 20, 23], which could explain the difference between predictions and experiments. Nevertheless, we ascribe this difference to the hypothesis of a constant dune shape and aspect ratio over time and to higher order of the speed-up effect. Indeed, finger dunes experience flows on either flank and the avalanche face flips from one side to the other as shown on figure 12 for a finger dune with $\theta = 150°$ and $N = 2$. Then, just after the plate rotation, the flow experiences an upwind slope close to the angle of repose. This is quite far from the assumption of a smooth profile with a small aspect ratio made by Jackson & Hunt [1]. Moreover, the dune shape progressively adapts to the flow and the upwind slope decreases, which makes the sediment flow decrease accordingly. Figure 13 shows, for the same sequence as figure 12, the sediment flux in the direction of the "undisturbed" flow (*i.e.* in the direction of the plate motion), averaged over the dune width, for a dune section midway from source. For each flow direction, the sediment flux is maximum during the first blow and decreases with time (as the upwind slope decreases). In addition,

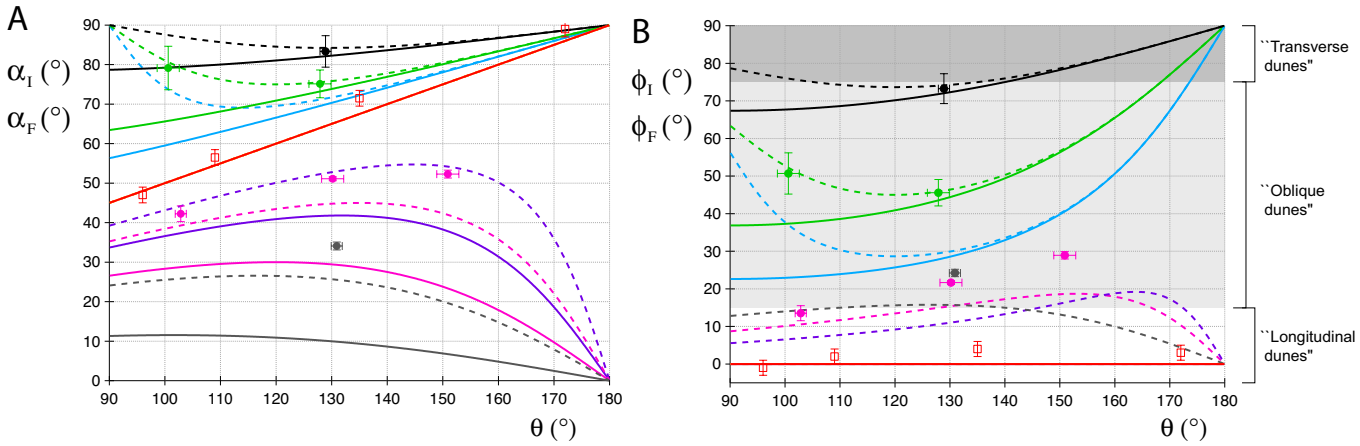

FIG. 11: Orientation of dunes in the experiments as a function of the divergence angle θ between flows. Curves show the model predictions for the bed instability mode with equations 5 ($\gamma = 0$, full lines) and 6 ($\gamma = \infty$, dashed lines) and for the fingering mode with equations 11 ($\gamma = 0$, full lines) and 12 ($\gamma = \infty$, dashed lines). Colours stand for time duration ratios N between flows. For the bed instability mode: red: $N = 1$, blue: $N = 1.5$, green: $N = 2$ and black: $N = 5$. For the fingering mode: orange: $N = 1$, pink: $N = 1.5$, violet: $N = 2$ and grey: $N = 5$. Circles are the experimental results of this study for asymmetric bimodal flow regimes. Empty squares show the orientations of dunes growing from a flat sand bed after 60 periods for symmetric flow regimes ($N = 1$) from Reffet *et al.* [26]. A: Orientation α_I and α_F of dune trends with respect to the prevailing flow direction in the two modes as a function of the divergence angle θ. B: Orientation Φ_I and Φ_F of dune trends with respect to the flow resultant (mean flux direction on a flat ground) in the two modes as a function of the divergence angle θ. Dunes whose orientation are higher (resp. smaller) than 45° are rather perpendicular (resp. parallel) to the resultant. Grey areas delimitate dune orientation ranges upon the "classical" denomination for dunes regarding their orientation with the resultant [2]. Dunes in the bed instability mode can be transverse, oblique or longitudinal. Finger dunes can only be longitudinal or oblique.

for a given time after the rotation, the sediment flux is bigger for the subdominant flow than for the prevailing flow. This is consistent with a bigger speed-up effect for the direction of the subdominant flow. Indeed, the direction of the subdominant flow makes an angle of 97.5° with the dune orientation, while the prevailing flow makes an angle of 52.5° with it. When taking into account only these measured sediment fluxes in the direction of the "undisturbed" flows, one finds a sediment flux direction $\alpha = 53.6° \pm 4°$, very close to the dune orientation $\alpha_F = 52.3° \pm 1°$. As a result, the deflection of the sediment flux appears here to have an incidental impact on the dune orientation. The sediment flux is calculated by integrating the height difference between successive dune profiles ($\partial q/\partial x = -\partial h/\partial t$), setting the sediment loss (that escapes from the dune) to zero for noise reduction. This correction may slightly change the results.

The hypothesis of a smooth dune profile with a small aspect ratio that does not change over time is not fulfilled in the experiments. This explains the underestimation of finger dune orientations with the prevailing flow. Note that it seems to have less impact on the orientation of dunes growing from the bed instability. This can be explained by the bigger size of dunes in the bed instability mode (by a factor 5 at the end of the experiment) than in the fingering mode, so that their avalanche face does not flip completely. This is also consistent with the experimental results of Walker and Nickling who measured a smaller "speed-up" effect for closely spaced transverse dunes than for isolated ones [13]. Reversing linear dunes in the field are mostly big dunes whose flipping avalanche face is constrained to a small region at the crest [29, 30]. Moreover, the wind orientations are usually distributed over a range, which makes the dune profile adapt more progressively than within a strict bimodal wind regime. Thus, the hypothesis of a constant dune shape over a period time (year) is much more valid for dunes in the field. Moreover, as shown in table I, the "speed-up" effect plays a minor role in dune orientation when flow directions are widely spread like in natural conditions.

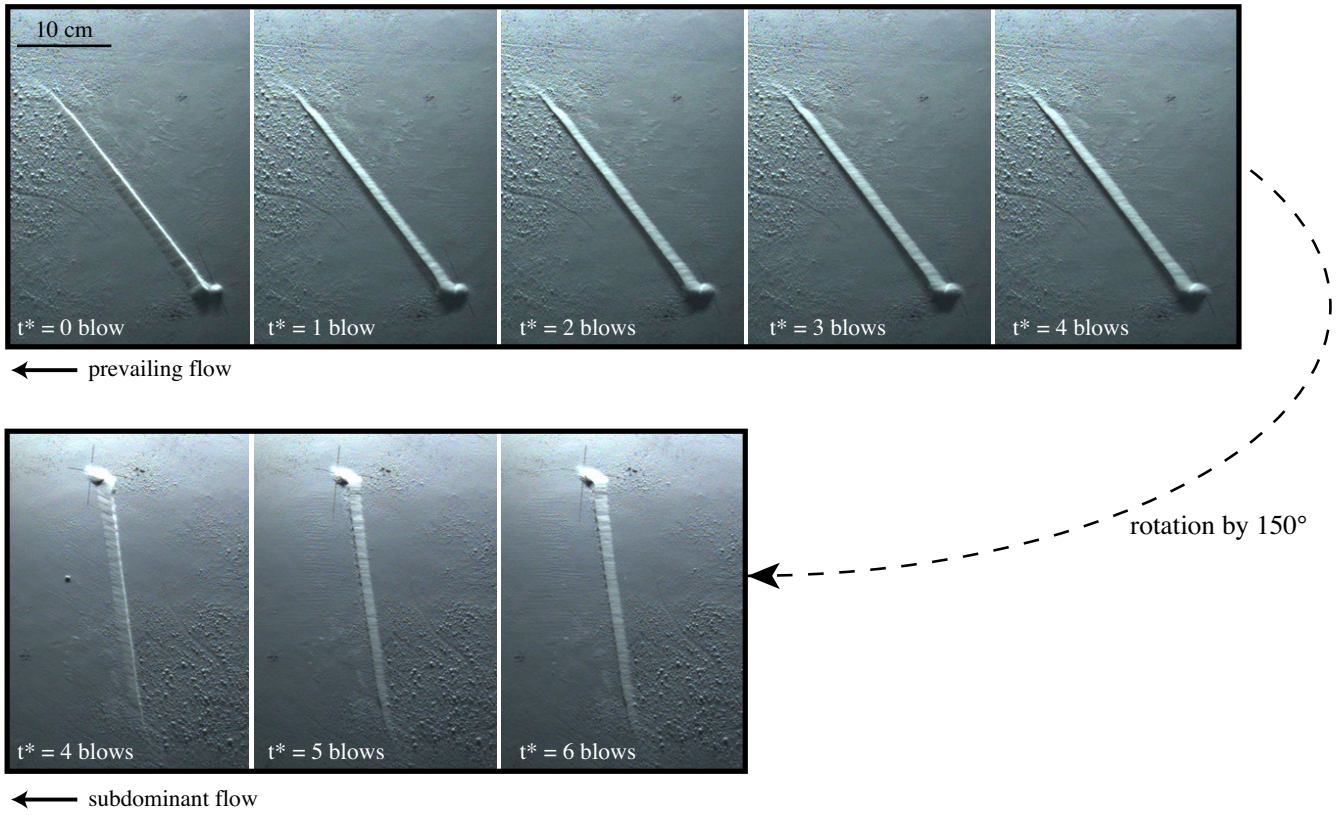

FIG. 12: Sequence of snapshots showing the finger dune before and after each blow. All images have the same scale. The fluid flow is from right to left, $\theta = 150^\circ$ and $N = 2$. The sequence shows the dune after 1038 blows (173 periods), $t^* = t - 1038$. One sees that the avalanche face flips from one side to the other and that the sediment flux during the first blow after the rotation is much bigger than the ones during the following blows.

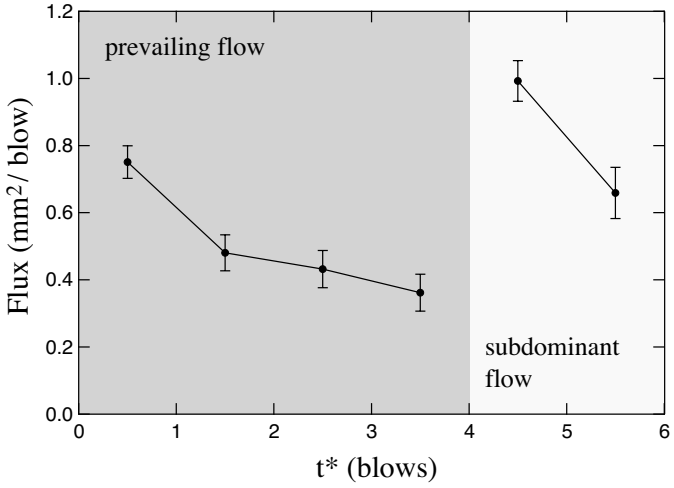

FIG. 13: Mean sediment flux over a finger dune section in the direction of the "undisturbed flow" as a function of time for a full period. Experiment parameters are $\theta = 150^\circ$ and $N = 2$. The sediment fluxes are averaged over a 20 mm section, midway from source. The sequence starts at time $t = 1038$ blows with the 4 blows of the prevailing flow followed by the 2 blows of the subdominant flow.

III. FIELD

We compare our model to dune orientation in the field. To do so, we collect wind data from a freely available assimilation system [31] and calculate the corresponding sediment fluxes and predicted orientations. These orientations are compared to dune orientation measured from satellite images provided by Google Earth.

We restrict our study to dune fields in North-Africa and China:

- where wind regimes are multimodal, *i.e* where the two modes of orientation may occur,
- where we can be confident that wind data corresponding to a given location apply to the dune field nearby, *i.e* where the predictions of α_I and α_F are not changing much between two adjacent points at the resolution scale of the wind data base (not too close to reliefs for example),
- and where the RDP/DP is reasonably high. Indeed, multiple dune orientations are possible for small RDP/DP values.

A. Wind data and estimation of the sand flux

The European Centre for Medium-Range Weather Forecasts (ECMWF) develops and maintains the Integrated Forecast System (IFS), a global meteorological forecasting model. Here, we use the outputs of its latest global atmospheric reanalysis project: the ERA-Interim-project [31]. This assimilation system aims to include all available and appropriate observational data from weather station, radiosonde, ship or satellite measurements. It provides data from the beginning of 1979 up to now with an horizontal spatial resolution of $0.75^\circ \times 0.75^\circ$ (about 83 km on the equator) and a time resolution of 6 hours (τ).

From the data set, which contains all important atmospheric parameters, we extract, for each time step i, the wind direction $\vec{x}_i$, and the wind speed u_i, 10 meters above the ground. Then, we calculate the shear velocity $u_{*,i}$, which is the relevant wind velocity for sediment transport:

$$u_{*,i} = \frac{u^i \kappa}{\ln(z/z_0)} \tag{13}$$

where $\kappa = 0.4$ is the von-Kármán constant, z the height at which the wind speed has been computed (10 meters here), and $z_0 = 10^{-3}$ m the surface roughness length scale. The value of the roughness z_0 depends on u_* as, in transport conditions, z_0 is controlled by the transport layer thickness. However, for z_0 typically ranging between 10^{-4} m and 2 10^{-3} m, $\ln(10/z_0)$ does not change much and ranges between 11.5 and 8.5.

In the last decades, many sand transport relations have been derived from analytical and phenomenological considerations thanks to wind-tunnel experiments [17, 32–40]. In all these relations, the sand flux increases with u_* and in most of them the wind cannot transport grains when u_* is smaller than a threshold velocity u_{*c}. They mainly differ by their scaling in u_* and $(u_* - u_{*c})$. Duran *et al.* [40], Andreotti [37] and Ho *et al.* [41] have shown from numerical simulations and wind tunnel experiments that the saturated sand flux, *i.e.* the sand flux at equilibrium over a flat sand bed, scales as $(u_*^2 - u_{*c}^2)$ for small u_* (when $u_* \lesssim 5u_{*c}$) and as u_*^3 for higher u_* values. Most of transport laws do scale with u_*^3 for high u_* as suggested by Bagnold [32]. However, the wind velocity values we consider rarely overpass 5 u_{*c}. In this range of wind velocities, wind tunnel data from Iversen and Rasmussen [35] find a good agreement with the relation proposed by Ungar & Haff [17], calibrated by Duran *et al.* [40]:

$$Q = 25\,\frac{\rho_f}{\rho_s}\sqrt{\frac{d}{g}}\left(u_*^2 - u_{*c}^2\right), \tag{14}$$

which is the relation we use to calculate Q, the saturated volumic sand flux per unit of length. In equation 14, ρ_f is the air density, ρ_s the sand density (we take a bulk or dune density equal to 0.6 ρ_s), g is the acceleration of gravity and d the grain size.
The threshold velocity u_{*c} is calculated with the relation:

$$u_{*c} = 0.1\sqrt{\frac{\rho_s g d}{\rho_f}}, \tag{15}$$

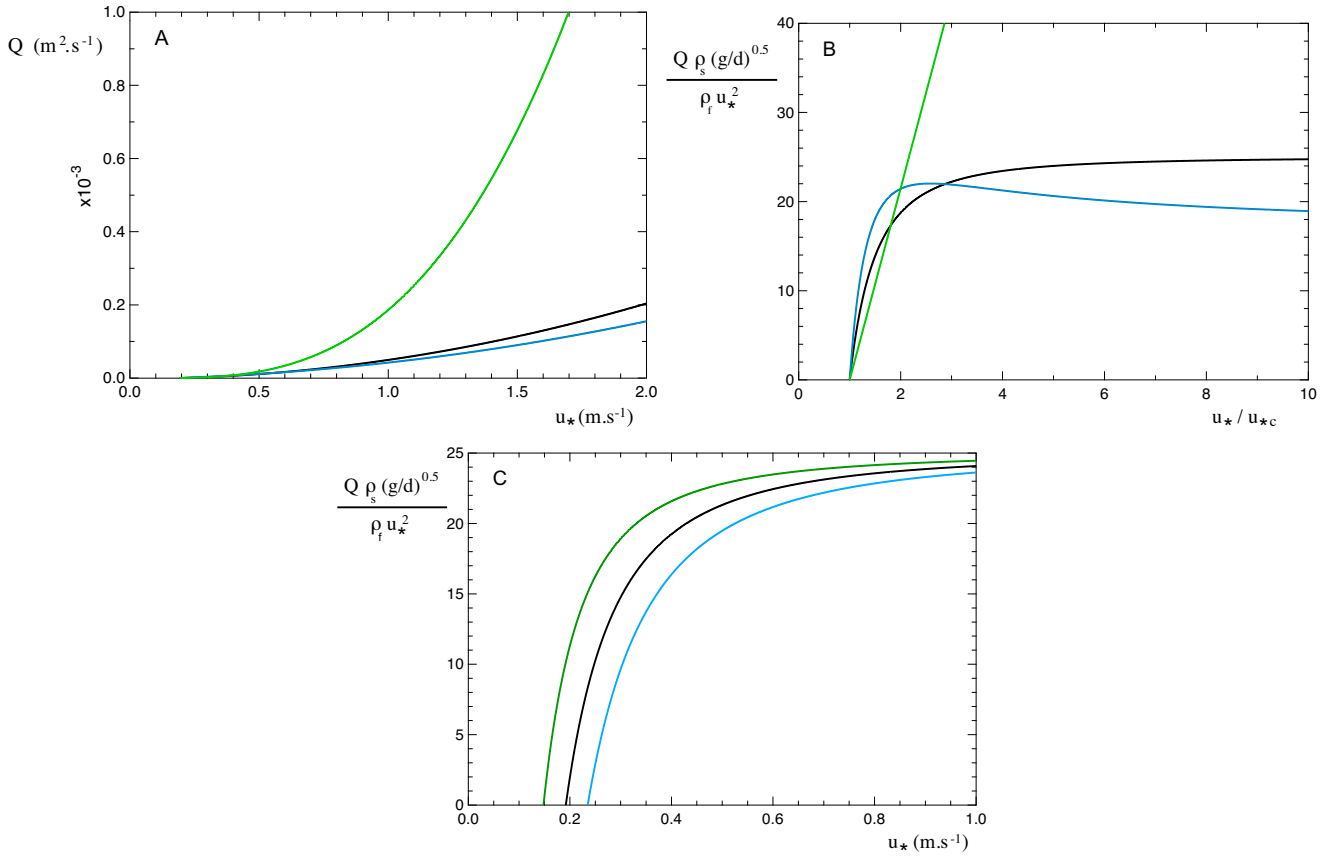

FIG. 14: The different transport laws. A: Sediment flux Q as a function of the shear velocity u_*, for $u_{*c} \simeq 0.19$ m.s^{-1}. Black: Ungar's transport law (eq. 14), blue: Sorensen's transport law (eq. 18), green: Lettau & Lettau's transport law (eq. 17). B: Same as in fig.A but Q and u_* are non-dimensionalised. It shows the scalings of the transport laws. C: Non-dimensional sediment flux of Ungar's law (eq. 14) for different onset velocity u_{*c}. Green: $u_{*c} \simeq 0.15$ m.s^{-1}, black: $u_{*c} \simeq 0.19$ m.s^{-1}, blue: $u_{*c} \simeq 0.23$ m.s^{-1}.

calibrated by Iversen *et al.* [42]. In all our calculations, we took $d = 180$ μm, for which $u_{*c} \simeq 0.19\,\mathrm{m.s^{-1}}$. Ten meters above the ground, it corresponds to a wind velocity $u_{10,\,c} \simeq 4.4$ m.s^{-1}.
For each time step we then calculate the saturated sand flux vector over a flat sand bed:

$$\overrightarrow{Q_i} = \begin{cases} Q_i \overrightarrow{x_i} & \text{for } u_{*,i} \geq u_{*c}, \\ 0 & \text{for } u_{*,i} < u_{*c}, \end{cases} \tag{16}$$

where $Q_i = Q(u_* = u_{*,i})$ using equations 14, 15 and 13.

The calculation of dune orientation does not depend on pre-factor values in the transport law but only on u_* and u_{*c} scalings and u_{*c} value. For comparisons and sensitivity tests, we also calculate the sand flux using the relation of Lettau and Lettau [34, 39]:

$$Q = 4.7\,\frac{\rho_f}{g\rho_s} u_*^2 (u_* - u_{*c}), \tag{17}$$

and the formula proposed by Sorensen [36]:

$$Q = \frac{\rho_f}{0.6\rho_s g} u_* (u_*^2 - u_{*c}^2) \left[A_S \left(\frac{u_{*c}}{u_*} \right)^2 + B_S \frac{u_{*c}}{u_*} \right], \tag{18}$$

where A_S and B_S depend on grain diameter d. When A_S and B_S are calibrated with transport rates obtained by Iversen and Rasmussen [35]: $A_S = 3.1$ and $B_S = 2.2$ for $d = 180\mu$m. The pre-factor value in equation 17 has been

set to be consistent with equation 18 thanks to the comparison made by Sherman and Li [39]. The dependency on the transport onset velocity has been investigated by changing $u_{10,\,c}$ value by 1 $\mathrm{m.s^{-1}}$ ($u_{10,\,c} \simeq 3.4$ and 5.4 $\mathrm{m.s^{-1}}$). To give an order of magnitude, these values correspond to onset velocities for $d \simeq 100\,\mu\mathrm{m}$ ($u_{*c} = 0.15\,\mathrm{m.s^{-1}}$) and $d \simeq 270\,\mu\mathrm{m}$ ($u_{*c} = 0.23\,\mathrm{m.s^{-1}}$), using equation 15. Fig. 14 compares the different transport laws (equations 14, 17 and 18) with $u_{*c} \simeq 0.19\,\mathrm{m.s^{-1}}$ and shows the influence of the threshold wind velocity on the estimation of sand flux (equation 14). As expected, the threshold wind velocity is only important for wind speeds close to the onset. Note that Q in equation 17 scales almost as u_*^3 when equations 18 and 14 scale as u_*^2.

From the individual flux vectors $\overrightarrow{Q_i}$, we estimate the drift potential DP, which is the sand flux averaged over the whole time period (~ 35 years):

$$\mathrm{DP} = \sum_{\mathrm{i=1}}^{\mathrm{N}} \|\overrightarrow{Q_i}\|\,\tau\,/\,\mathrm{T},$$

where τ ($\tau = 6$ hours) is the time duration between two consecutive wind data i and T ($T = N\tau \simeq 35$ years) the whole duration of the considered data set. We also calculate the resultant drift potential RDP:

$$\mathrm{RDP} = \left|\left|\sum_{\mathrm{i=1}}^{\mathrm{N}} \tau\,\overrightarrow{Q_i}\right|\right| / \,\mathrm{T}.$$

DP is the sum of the norm of all the transport vectors over time while RDP is the norm of the sum of all these transport vectors. The ratio RDP/DP is a dimensionless number often used to estimate sand transport directionality, independently of wind strength. When RDP/DP $\rightarrow 1$, the wind regime tends to be unidirectional, when RDP/DP $\rightarrow$ 0 the resultant sand flux is null. Such a value is observed in zones of multidirectional wind regimes or in zones where two winds have opposite directions.

B. Estimation of the divergence angle

The divergence angle ϕ accounts for the range of the sand flux orientations. For a bimodal wind regime, one can define the divergence angle to be the angle between the two wind directions. The divergence angle is then independent of the DP value. However, for a multimodal or a natural wind regime, the divergence angle cannot be defined independently of the DP value. We define it as 2 times the standard deviation of fluxes distribution around the mean flux direction (RDD):

$$\phi = 2\sqrt{\frac{\int_0^{2\pi} \|\overrightarrow{Q}(\theta)\|\eta^2 d\theta}{\int_0^{2\pi} \|\overrightarrow{Q}(\theta)\| d\theta}}, \tag{19}$$

where $\|\overrightarrow{Q}(\theta)\|$ is the drift potential in the direction θ and η is the difference between the flux direction θ and the mean sand flux direction (RDD). This definition is a classical standard deviation definition with weighted distribution values.

C. Prediction of dune orientations

The angles associated with the different modes of dune orientation can be derived numerically from the sand flux data $\overrightarrow{Q_i}$. All the angles are measured anti-clockwise from the East.
To find the orientation corresponding to the bed instability mode, we first calculate the total growth rate $\sigma(\alpha)$ for all possible dune orientations $\alpha \in [0;\,\pi]$. The vector flux $\overrightarrow{Q_i}$ makes an angle θ_i with the East, so that:

$$\sigma(\alpha) \propto \frac{\sum_{i=1}^{N} \|\overrightarrow{Q_i}\| \left[|\sin(\alpha-\theta_i)| + \gamma \sin^2(\alpha-\theta_i)\right] \tau}{T}. \tag{20}$$

To have the dimension of a typical growth rate ($\mathrm{T^{-1}}$), equation 20 should be divided by the characteristic cross section area of the dune HW. γ stands for the speed-up effect, which is taken proportional to the dune aspect ratio

experienced by the wind of orientation θ_i. The bed instability orientation σ_i is then the α value for which σ is maximum (eq. 20).

The orientation of the fingering mode α_F is the one of the mean sand flux, which is perturbed by the dune. Then, α_F is such that the direction of the mean sand flux $\vec{Q}_{\rm d}$ corresponds to the one of the dune, with:

$$\vec{Q}_{\rm d}(\alpha) = \sum_{i=1}^{N} \|\overrightarrow{Q_i}\| \left(1+\gamma|\sin(\alpha-\theta_i)|\right) \left(\cos\theta_i\,\vec{i} + \sin\theta_i\,\vec{j}\right) \tau \;/\; T, \tag{21}$$

where $\vec{i}$ and $\vec{j}$ are unit vectors pointing respectively towards the East and the North. In practice, α_F is such that the sediment flux perpendicular to the dune $Q_{\rm d\,\perp}(\alpha)$ is null and the flux parallel to it $Q_{\rm d\parallel}(\alpha)$ is positive, with:

$$Q_{\rm d\,\perp}(\alpha) = \frac{\displaystyle\sum_{i=1}^{N} \|\overrightarrow{Q_i}\| \left(1+\gamma|\sin(\alpha-\theta_i)|\right) \sin(\alpha-\theta_i)\tau}{T}, \tag{22}$$

and

$$Q_{\rm d\,\parallel}(\alpha) = \frac{\displaystyle\sum_{i=1}^{N} \|\overrightarrow{Q_i}\| \left(1+\gamma|\sin(\alpha-\theta_i)|\right) \cos(\alpha-\theta_i)\tau}{T}. \tag{23}$$

As discussed in the model section, γ typically ranges between 0.5 and 2 and we take $\gamma = 1$ for all field calculations.

D. Orientation of dunes in the field

The dune orientations are measured from top view images provided by Google Earth in the vicinity of the wind rose coordinates. As shown on figure 15, we first calculate the auto-correlation of dune field images (figs. 15 A1 and B1). The auto-correlation is maximum along the direction in which the image is unaffected by a translation. Thus, the direction of maximum auto-correlation gives the dune orientation. The value of the auto-correlation as a function of direction is calculated by summing the auto-correlation value on a segment, which starts at the auto-correlation image center and whose length equals two wave lengths, and which is rotated by steps of one degree. We do this measurement for several areas of the field and calculate the average and the standard deviation. The dune orientations are measured counterclockwise with respect to the East. Orientations corresponding to the bed instability mode and the fingering mode are defined modulo 2π and π respectively. Aside from their orientation, dunes often exhibit two different length scales for their width or wavelength: a small one of about 30 m and a large one of the order of 1 km. Thus, we measure their corresponding orientations separately. Given the time scale of ERA-Interim data ($\sim$ 30 years), predictions should be compared to the orientation of small scale dunes. However, as shown in table I dunes orientation within a given mode, does not vary significantly with length scale. It suggests that the 30 year data from the ERA-Interim project give a right picture of the wind regime that builds these sand seas.

Figures 16 to 26 show wind data and compare predictions to observations for 11 dune fields. Measurements were made on larger areas than the ones on figures. Table I summarizes field studies. It shows the drift potential DP, the ratio RDP/DP, the divergence angle ϕ, the predictions α_I and α_F and the corresponding measured values for all considered dune fields. Table I gives the values of predicted α_I and α_F for γ equal to 0, 1 and $+\infty$. Depending on γ value, α_I only changes by a couple of degrees, but α_F can differ by 10°. Setting γ to 1 often gives a mid-range value for orientations. Two different uncertainty ranges are shown for predicted angles. The first one corresponds to the variation when changing the transport onset velocity in Ungar & Haff transport law (eq. 14). The second one corresponds to the variation when changing the transport law (eq. 17 and 18) with $u_{*c} \simeq 0.19\,m.s^{-1}$.

Big dunes in the sand seas we consider (figs. 16 to 26) mostly exhibit an orientation that corresponds to the fingering mode. Although wind regime may have changed since they formed, the fingering growth is definitely at play in the field as shown by the fingering mode orientation of small modern dunes (*e.g.* fig. 16). As a result, this new

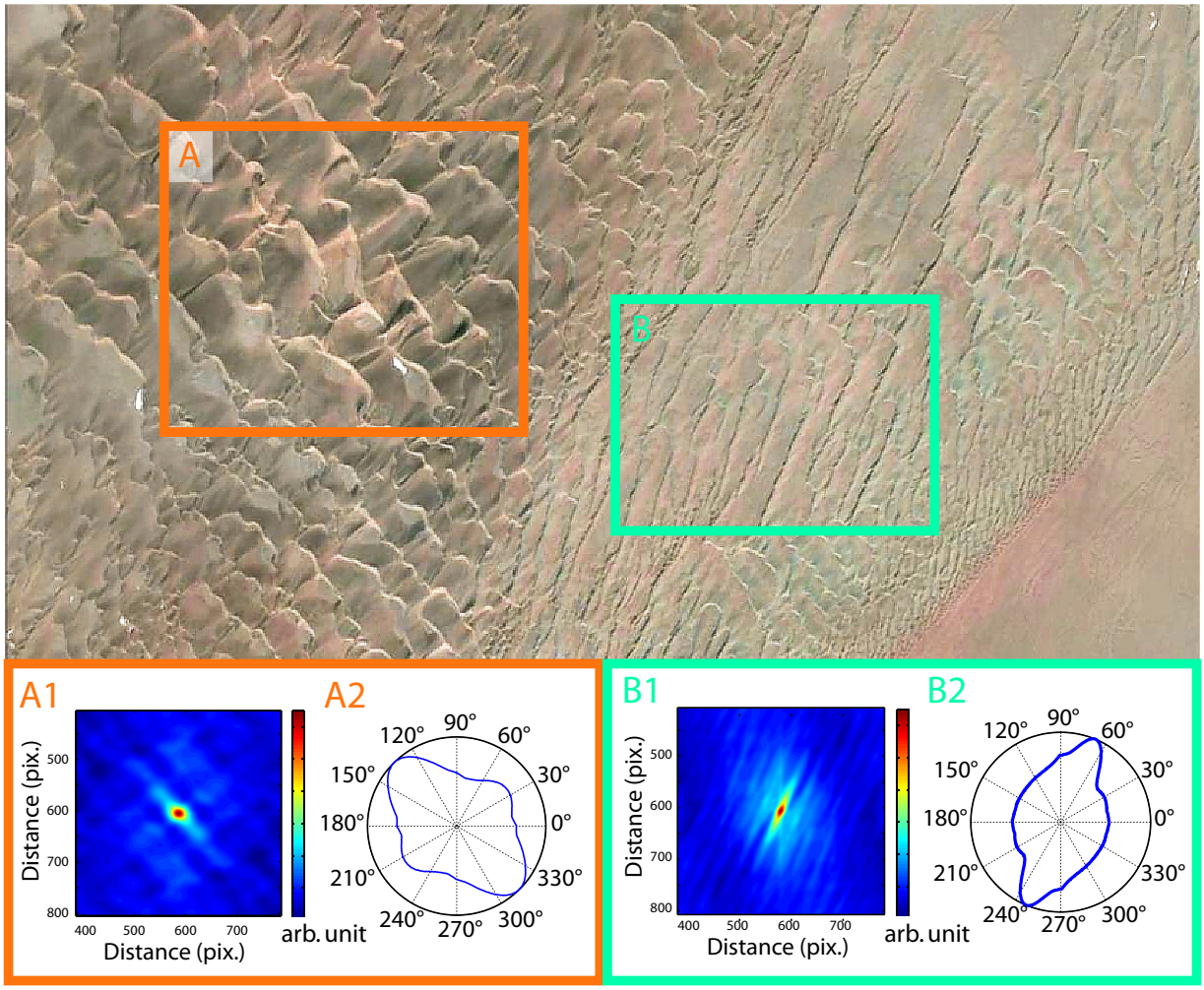

FIG. 15: Method for the calculation of dune orientation. The top image shows a dune field in the South Taklamakan (from Google Earth, 38.32° N, 86.67° E). Figures A1 and B1 show the auto-correlation of framed areas A and B. Figures A2 and B2 show the auto-correlation value as as function of the direction. Here the peaks give 134° for the bed instability mode (A2) and 248° for the fingering mode (B2). Averaged values for the dune field are 142.6° ±7° for the bed instability mode and 250.8° ±3° for the fingering mode. One notices a smaller secondary peak in figure A2, which corresponds to the defects alignment.

orientation should be considered when using the orientation of dunes as a proxy for wind regime [43–50].

[1] P.S. Jackson and J.C.R. Hunt. Turbulent wind flow over a low hill. *Quart. J. R. Met. Soc.*, 101:929–955, 1975.

[2] D. M. Rubin and R. E. Hunter. Bedform alignment in directionally varying flows. *Science*, 237:276–278, 1987.

[3] B. Andreotti, P. Claudin, and S. Douady. Selection of dune shapes and velocities part 2: A two-dimensional modeling. *The european physical Journal B*, 28:341–352, 2002.

[4] D. Zhang, C. Narteau, O. Rozier, and S. Courrech du Pont. Morphology and dynamics of star dunes from numerical modelling. *Nature Geoscience*, 5:463–467, 2012.

[5] H. Tsoar. Profile analysis of sand dunes and their steady state significance. *Geografiska Annaler*, 67A:47–59, 1985.

[6] N. Lancaster. Variations in wind velocity and sand transport on the windward flanks of desert sand dunes. *Sedimentology*, 32:591–593, 1985.

[7] W. Gong and A. Ibbetson. A wind tunnel study of turbulent flow over model hills. *Boundary-Layer Meteorology*, 49:113–148, 1989.

[8] J.J. Finnigan, M.R. Rauchpach, E.F. Bradley, and G.K. Aldis. A wind tunnel study of turbulent flow over a two-dimensional ridge. *Boundary-Layer Meteorology*, 50:277–317, 1990.

[9] S.M Arens, H.M.E. Van Kaam-Peters, and J.H. Van Boxel. Air flow over foredunes and implications for sand transport. *Earth Surface Processes and Landforms*, 20:315–332, 1995.

[10] N. Lancaster, W.G. Nickling, C.K. McKenna Neuman, and V.E. Wyatt. Sediment flux and airflow on the stoss slope of a barchan dune. *Geomorphology*, 17:55–62, 1996.

[11] C. McKenna Neuman, N. Lancaster, and W. Nickling. Relations between dune morphology, air flow, and sediment flux on reversing dunes, silver peak, nevada. *Sedimentology*, 44:1103–1113, 1997.

[12] I.J. Walker and W.G. Nickling. Dynamics of secondary airflow and sediment transport over and in the lee of transverse dunes. *Progress in Physical Geography*, 26:47–75, 2002.

[13] I.J. Walker and W.G. Nickling. Simulation and measurement of surface shear stress over isolated and closely spaced transverse dunes in a wind tunnel. *Earth Surface Processes and Landforms*, 28:1111–1124, 2003.

[14] M.C. Baddock, I. Livingstone, and G.F.S. Wiggs. The geomorphological significance of airflow patterns in transverse dune interdunes. *Geomorphology*, 87:332–336, 2007.

[15] I.J. Walker, P.A. Hesp, R.G.D. Davidson-Arnott, B.O. Bauer, S.L. Namikas, and J. Ollerhead. Response of three-dimensional flow to variations in the angle of incident wind and profile form of dunes: Greenwich dunes, prince edward island, canada. *Geomorphology*, 105:127–138, 2009.

[16] P. Claudin, G.F.S. Wiggs, and B. Andreotti. Field evidence for the upwind velocity shift at the crest of low dunes. *Boundary-Layer Meteorology*, 148:195–206, 2013.

[17] J.E. Ungar and P.K. Haff. Steady state saltation in air. *Sedimentology*, 34:289–299, 1987.

[18] R.E. Hunter, B.M. Richmond, and T.R. Alpha. Storm-controlled oblique dunes of the oregon coast. *Bul. Geol. Soc. Am.*, 94:1450–1465, 1983.

[19] H. Tsoar. Dynamic processes acting on a longitudinal (seif) sand dune. *Sedimentology*, 30(4):567–578, 1983.

[20] H. Tsoar and D.H. Yaalon. Deflection of sand movement on a sinuous longitudinal (self) dune: use of fluorescent dye as tracer. *Sedimentary Geology*, 36:25–39, 1983.

[21] M.L. Sweet and G. Kocurek. An empirical model of aeolian dune lee-face airflow. *Sedimentology*, 37:1023–1038, 1990.

[22] P.A. Hesp, R. Davidson-Arnott, I.J. Walker, and J. Ollerhead. Flow dynamics over a fore dune at prince edward island, canada. *Geomorphology*, 65:71–84, 2005.

[23] I.J. Walker and D.H. Shugar. Secondary flow deflection in the lee of transverse dunes with implications for dune morphodynamics and migration. *Earth Surface Processes and Landforms*, 2013.

[24] K. Kroy, G. Sauermann, and H.J. Herrmann. Minimal model for sand dunes. *Phys. Rev. Lett.*, 88:054301, 2002.

[25] P. Hersen, S. Douady, and B. Andreotti. Relevant length scale for barchan dunes. *Phys. Rev. Lett.*, 89(26), 2002.

[26] E. Reffet, S. Courrech du Pont, P. Hersen, and S. Douady. Formation and stability of transverse and longitudinal sand dunes. *Geology*, 39(6):491–494, 2010.

[27] E.J.R. Parteli, J.S. Andrade, and H.J. Herrmann. Transverse instability of dunes. *Phys. Rev. Lett.*, 107:188001, 2011.

[28] L. Guignier, H. Niiya, H. Nishimori, D. Lague, and A. Valance. Sand dunes as migrating strings. *Phys. Rev E*, 87:052206, 2013.

[29] N. Lancaster. Linear dunes. *Prog. Phys. Geogr.*, 6:475–504, 1982.

[30] K. Pye and H. Tsoar. *Aeolian Sand And Sand Dunes.* Unwin Hyman, London, 1990.

[31] D.P. Dee and 35 others. The era-interim reanalysis: configuration and performance of the data assimilation system. *Q. J. R. Meteorological Society*, 137:553–597, 2001.

[32] R.A. Bagnold. The transport of sand by wind. *Geographical Journal*, 89:409–438, 1937.

[33] P.R. Owen. Saltation of uniform grains in air. *J. Fluid Mech.*, 20:225–242, 1964.

[34] K. Lettau and H.H. Lettau. *Experimental and micro-meteorological field studies of dune migration.* 1978.

[35] J. D. Iversen and K. R. Rasmussen. The effect of wind speed and bed slope on sand transport. *Sedimentology*, 46:723–731, 1999.

[36] M. Sørensen. On the rate of aeolian sand transport. *Geomorphology*, 59:53–62, 2004.

[37] B. Andreotti. A two species model of aeolian sand transport. *J. Fluid Mech.*, 510:47–70, 2004.

[38] O. Duràn and H. Herrmann. Modeling of saturated sand flux. *Journal of Statistical Mechanics: Theory and Experiment*, 2006.

[39] D.J. Sherman and L. Bailiang. Predicting aeolian sand transport rates: A reevaluation of models. *Aeolian Research*, 2011.

[40] O. Duràn, P. Claudin, and B. Andreotti. On aeolian transport: Grain-scale interactions, dynamical mechanisms and scaling laws. *Aeolian Research*, 3:243–270, 2011.

[41] T.D. Ho, A. Valance, P. Dupont, and A. Ould El Moctar. Scaling laws in aeolian sand transport. *Phys. Rev. Lett.*, 106:094501, 2011.

[42] J. D. Iversen, R. Greeley, J.R. Marshall, and J.B. Pollack. Aeolian saltation threshold: the effect of density ratio. *Sedimentology*, 34:699–706, 1987.

[43] N. Lancaster, G. Kocurek, A. Singhvi, V. Pandey, M. Deynoux, J.F. Ghienne, and K L. Late pleistocene and holocene dune activity and wind regimes in the western sahara desert of mauritania. *Geology*, 30:991–994, 2002.

[44] D.M. Rubin and P.A. Hesp. Multiple origins of linear dunes on earth and titan. *Nature Geoscience*, 2:653–659, 2009.

[45] N. Lancaster. Assessing dune-forming winds on planetary surfaces-application of the gross bed form normal concept. In *Second international planetary dunes workshop, Alamosa, Colorado*, 2010.

[46] M.C. Bourke, N. Lancaster, L.K. Fenton, E.J.R. Parteli, J.R. Zimbelman, and J. Radebaugh. Extraterrestrial dunes: An introduction to the special issue on planetary dune systems. *Geomorphology*, 121:1–14, 2010.

[47] R.C. Ewing, A.-P.B. Peyret, G. Kocurek, and M. Bourke. Dune field pattern formation and recent transporting winds in the olympia undae dune field, north polar region of mars. *J. Geophys. Res.*, 115:1–25, 2010.

[48] E. Eastwood, G. Kocurek, D. Mohrig, and T.. Swanson. Methodology for reconstructing wind direction, wind speed and duration of wind events from aeolian cross-strata. *Journal of Geophysical Research*, 117:F03,035, 2012.
[49] L.K. Fenton, T.I. Michaels, and R.A. Beyer. Inverse maximum gross bedform-normal transport 1: How to determine a dune-constructing wind regime using only imagery. *Icarus*, 230:5–14, 2013.
[50] M.W. Telfer and P.P. Hesse. Palaeoenvironmental reconstructions from linear dune fields: Recent progress, current challenges and future directions. *Quaternary Science Reviews*, 78:1–21, 2013.
[51] R. Cooke, A. Warren, and A. Goudie. *Desert Geomorphology*. UCL press., 1993.
[52] Z. Dong, J. Qu, X. Wang, G. Qian, W. Luo, and Z. Wei. Pseudo-feathery dunes in the kumtagh desert. *Geomorphology*, 100:328–334, 2008.
[53] Maximization or minimization arguments are often used in geomorphology. Although they might sound reasonable or intuitive, they often do not correspond to a physical principle. Here, this argument does correspond to a physical principle.
[54] Here the relationship between the wind velocity and the saturated sand flux neglects the existence of a transport onset. It is verified when the wind velocity is much bigger than the threshold velocity for transport.

Place & Coordinates	DP (m^2/year)	ϕ (°)	RDP/DP	$\alpha_{I,\gamma=0}$ (°)	$\alpha_{I,\gamma=\infty}$ (°)	$\alpha_{I,\gamma=1}$ (°)	$\alpha_{F,\gamma=0}$ (°)	$\alpha_{F,\gamma=\infty}$ (°)	$\alpha_{F,\gamma=1}$ (°)	α_I (field) (°)	α_F (field) (°)
Erg Chech-Adrar (Mali) (23.25°N, -5.25°E)	32.2	122	0.62 ± 0.02	115.5	116.7	116.2 ± 1 ± 0.3	225.8	235.5	230 ± 3 ± 1.3	117.6 ± 10	230.4 ± 7
Erg Chech-Adrar (Mali) (24°N, -5.25°E)	33.4	125	0.6 ± 0.02	109.8	111.6	110.9 ± 2 ± 0.4	225.1	235.3	229.7 ± 3 ± 1.4	112.8 ± 15	233.2 ± 1
Edeyen Ubari (Lybia) (27°N, 12.75°E)	23.7	170	0.32 ± 0.04	72.3	73.4	72.8 ± 1.5 ± 0.4	165.6	162.3	163.9 ± 5.5 ± 3.3	64.3 ± 8	157 ± 8
Great Sand Sea (Egypt) (25.5°N, 27°E)	11.5	132	0.57 ± 0.02	13.8	11.3	12.4 ± 7 ± 2.9	285.2	286.9	286 ± 10.5 ± 8.8	8.4 ± 6	285.1 ± 2
Great Sand Sea (Egypt) (26.25°N, 27°E)	11.6	135	0.53 ± 0.02	13.7	10.1	12 ± 9 ± 3.7	284.9	286.9	285.9 ± 11.5 ± 1.4	14.3 ± 5	285.9 ± 4
North of Abu Moharik (Egypt) (29.25°N, 29.25°E)	28.4	112	0.65 ± 0.01	9.2	3	4.8 ± 6 ± 4	291.3	295.6	293.4 ± 7.5 ± 5.2	-0.1 ± 8	294.2 ± 7
Rub'al Khali (Saudi Arabia) (19.5°N, 48°E)	12	133	0.52 ± 0.04	146	145.4	145.6 ± 8.5 ± 2.4	213	209.1	211.4 ± 11.5 ± 3.8	156.3 ± 4	205.9 ± 5
Rub'al Khali (Saudi Arabia) (19.5°N, 48.75°E)	12.3	139	0.46 ± 0.04	152.8	153.4	153.2 ± 6.5 ± 1.7	206.3	200.7	203.8 ± 8.5 ± 3	140 ± 7	202.6 ± 5
South Taklamakan (China) (38.25°N, 86.25°E)	8.4	125	0.62 ± 0.05	138.2	138.2	138.2 ± 5.5 ± 1.5	233.4	244.5	235.5 ± 12 ± 2.1	138.2 ± 3	232 ± 3
South Taklamakan (China) (38.25°N, 87°E)	3.8	134	0.52 ± 0.05	149.1	152.2	150.9 ± 13.5 ± 2.6	249.7	267.9	256.6 ± 12.5 ± 3.9	142.6 ± 7	250.8 ± 3
Mu Us (China) (39°N, 108°E)	26.5	152	0.44 ± 0.04	37.1	38.6	37.9 ± 1.5 ± 1.5	341.4	351.5	344.9 ± 5 ± 5	38.5 ± 4	not observed

TABLE I: Records of field studies. All calculations are made using the ERA-Interim wind data with Ungar & Haff transport law (eq. 14) with a threshold transport velocity $u_{*c} \simeq 0.19\,\mathrm{m.s^{-1}}$. RDP/DP is calculated for each year and average. The uncertainty range is the standard deviation. Uncertainty ranges associated to $\alpha_{I,\gamma=1}$ and $\alpha_{F,\gamma=1}$ show half the variation when changing the threshold velocity u_{*c} (from 0.15 to $0.23\,\mathrm{m.s^{-1}}$) and half the variation when changing the transport law with $u_{*c} \simeq 0.19\,\mathrm{m.s^{-1}}$. Note that $\alpha_{F,\gamma=0}$ is also the direction of the resultant drift potential.

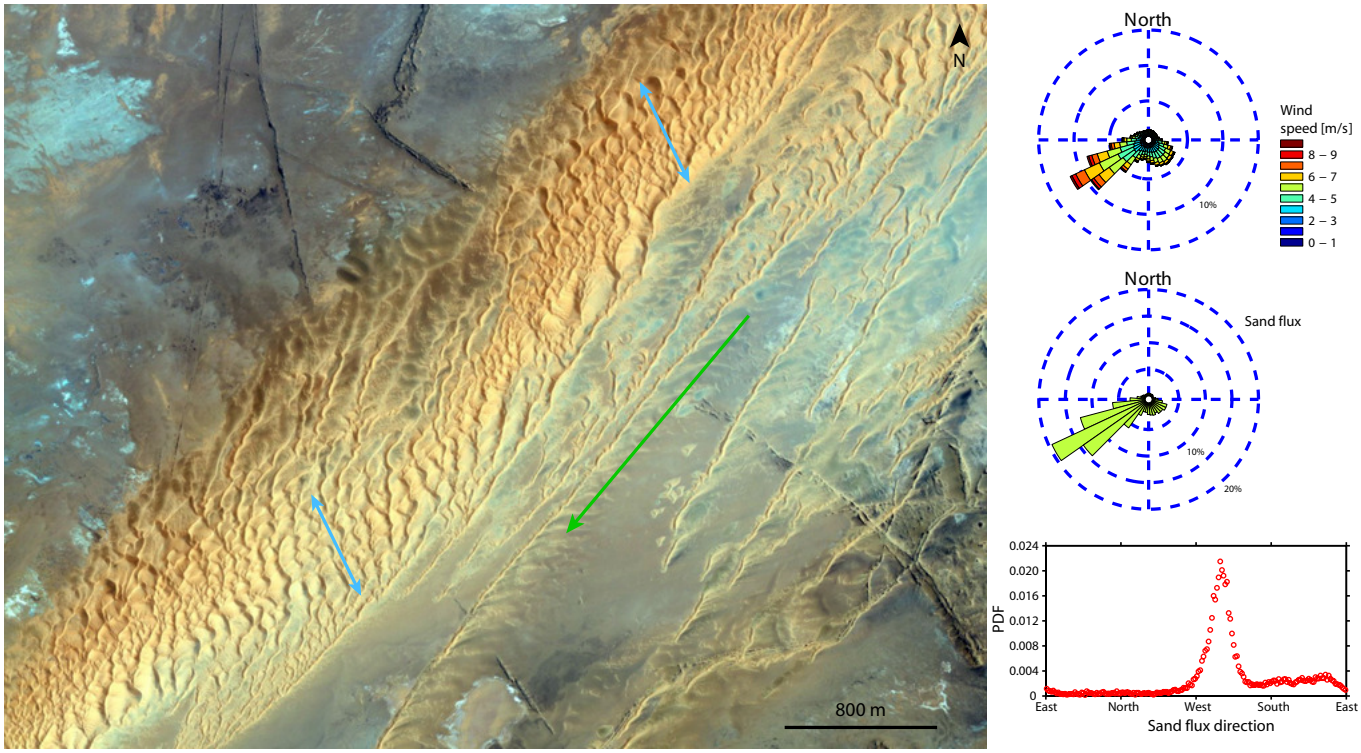

FIG. 16: Erg Chech-Adrar (Mali) view and corresponding sediment transport properties. Images come from Google Earth (23.56° N, −5.07° E). Coordinates of the wind rose are 23.25° N, −5.25° E. RDP/DP = 0.63 ± 0.02 and the divergence angle of flux is 122°. Blue arrows show the predicted orientation of the bed instability mode (116.2°). Green arrow shows the predicted orientation of the fingering mode (230°). Measured orientations are 117.6° ± 10.2° for the bed instability, 230.4° ± 1° for the fingering at small scale and 228.7° ± 2.3° for the fingering at large scale. Note that the coexistence of small dunes of similar size with two different orientations can not be ascribed to a temporal change of the wind regime.

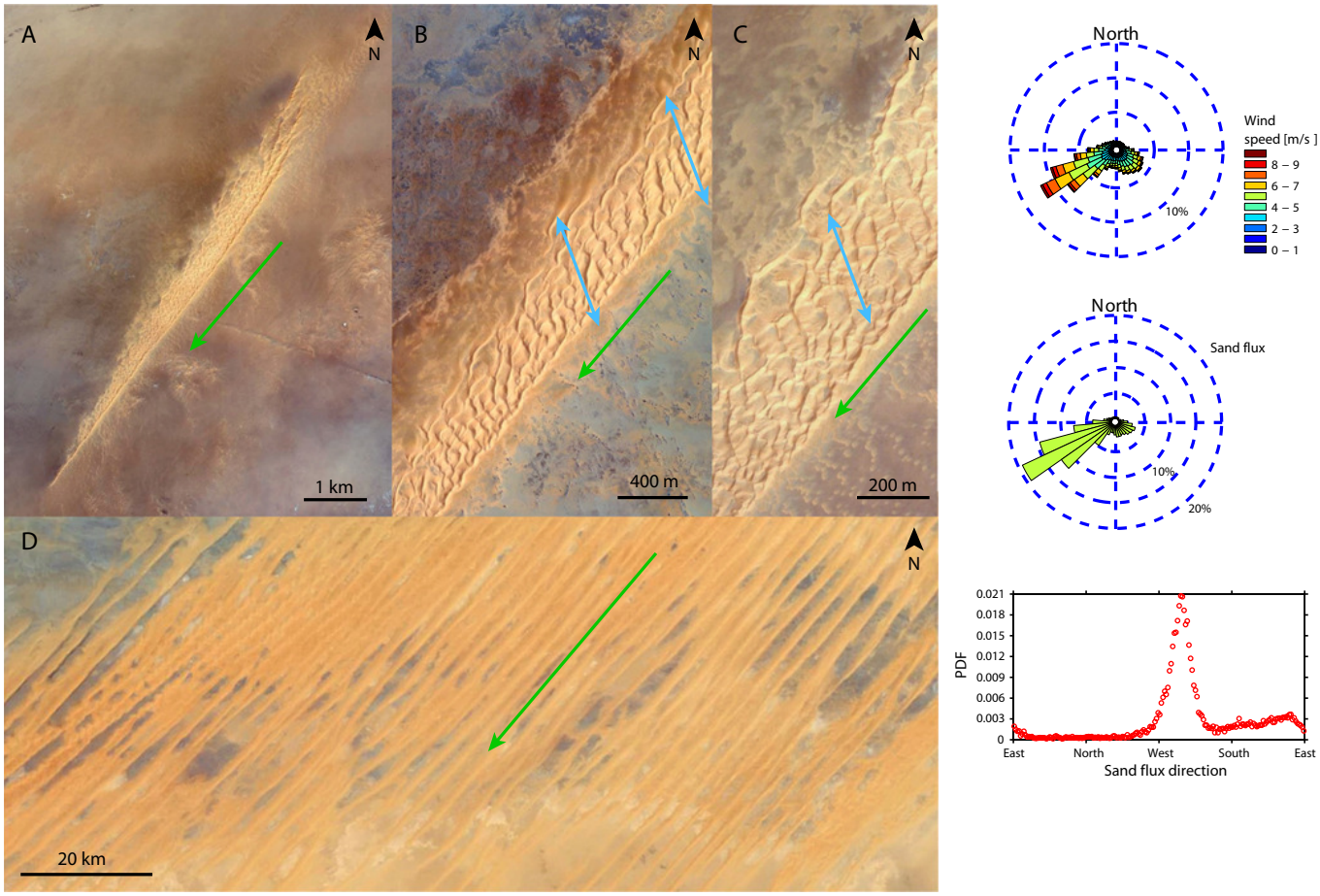

FIG. 17: Erg Chech-Adrar (Mali) views at different scales and corresponding sediment transport properties. Images come from Google Earth (A, B, C: 23.72° N, −4.94° E, D: 24.3° N, −4.67° E). Coordinates of the wind rose are 24° N, −5.25° E. RDP/DP $= 0.6 \pm 0.02$ and the divergence angle of flux is 125°. Blue arrows show the predicted orientation of the bed instability mode (110.9°). Green arrows show the predicted orientation of the fingering mode (229.7°). Measured orientations are 112.8° ± 15° for the bed instability mode, 233.2° ± 1° for the fingering at small scale and 228.7° ± 2.3° for the fingering at large scale. Note the barchans at the bottom of image C, which are aligned with the average flux direction, unlike the superimposed pattern on the big finger dune.

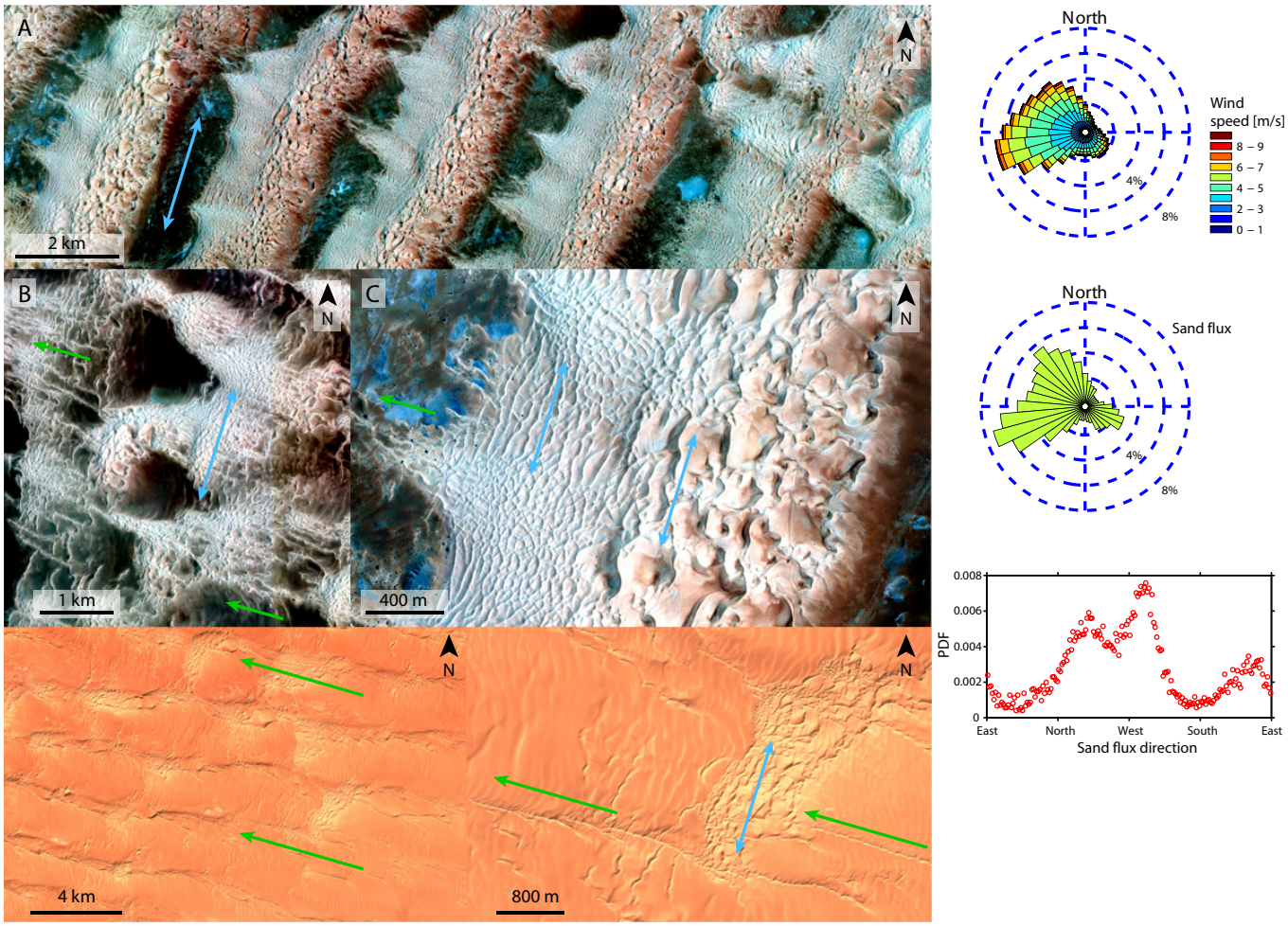

FIG. 18: Edeyen Ubari (Libya) views at different scales and corresponding sediment transport properties. Images come from Google Earth (A, B, C: 26.96° N, 12.99° E, D, E: 26.81° N, 12.64° E). Coordinates of the wind rose are 27° N, 12.75° E. RDP/DP = 0.32±0.04 and the divergence angle of flux is 170°. Blue arrow shows the predicted orientation of the bed instability mode (72.8°). Green arrow shows the predicted orientation of the fingering mode (163.9°). Measured orientations are 64.3°±8° for the bed instability at small scale, 59.4° ± 4.6° for the bed instability at large scale and 157° ± 8° for the fingering. The low-contrast bedforms seen in the inter-dune areas appear to be sand sheets of segregated coarse grains [30, 51, 52].

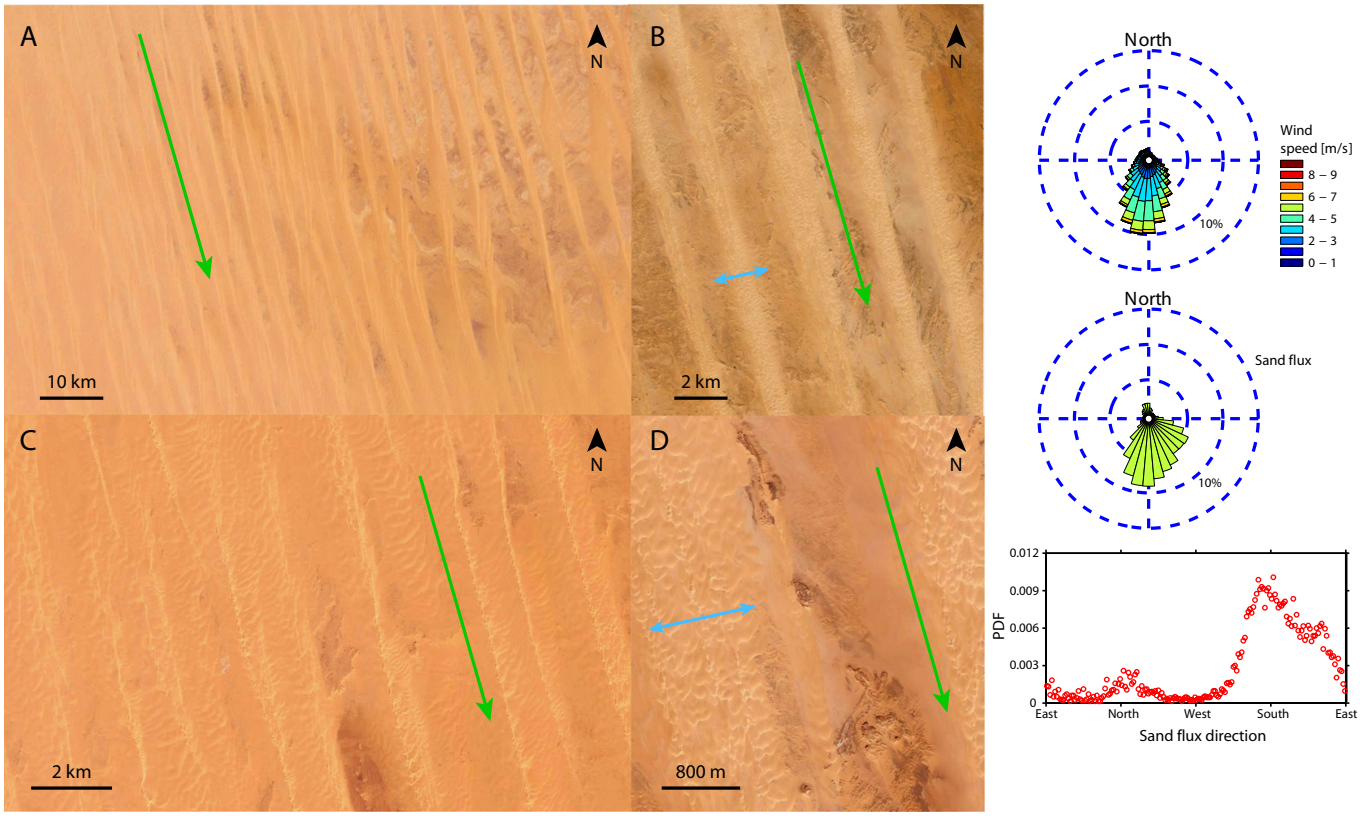

FIG. 19: Great Sand Sea (Egypt) views at different scales and corresponding sediment transport properties. Images come from Google Earth (A: 25.86° N, 26.70° E, B: 24.87° N, 27° E, C: 25.51° N, 26.77° E, D: 24.9° N, 27.08° E). Coordinates of the wind rose are 25.5° N, 27° E. RDP/DP $= 0.57 \pm 0.02$ and the divergence angle of flux is 132°. Blue arrow shows the predicted orientation of the bed instability mode (12.4°). Green arrow shows the predicted orientation of the fingering mode (286°). Measured orientations are $8.4° \pm 6°$ for the bed instability, $285.1° \pm 1.6°$ for the fingering at small scale and $284.7° \pm 1.5°$ for the fingering at large scale. The low-contrast bedforms seen in the inter-dune areas appear to be sand sheets of segregated coarse grains [30, 51, 52].

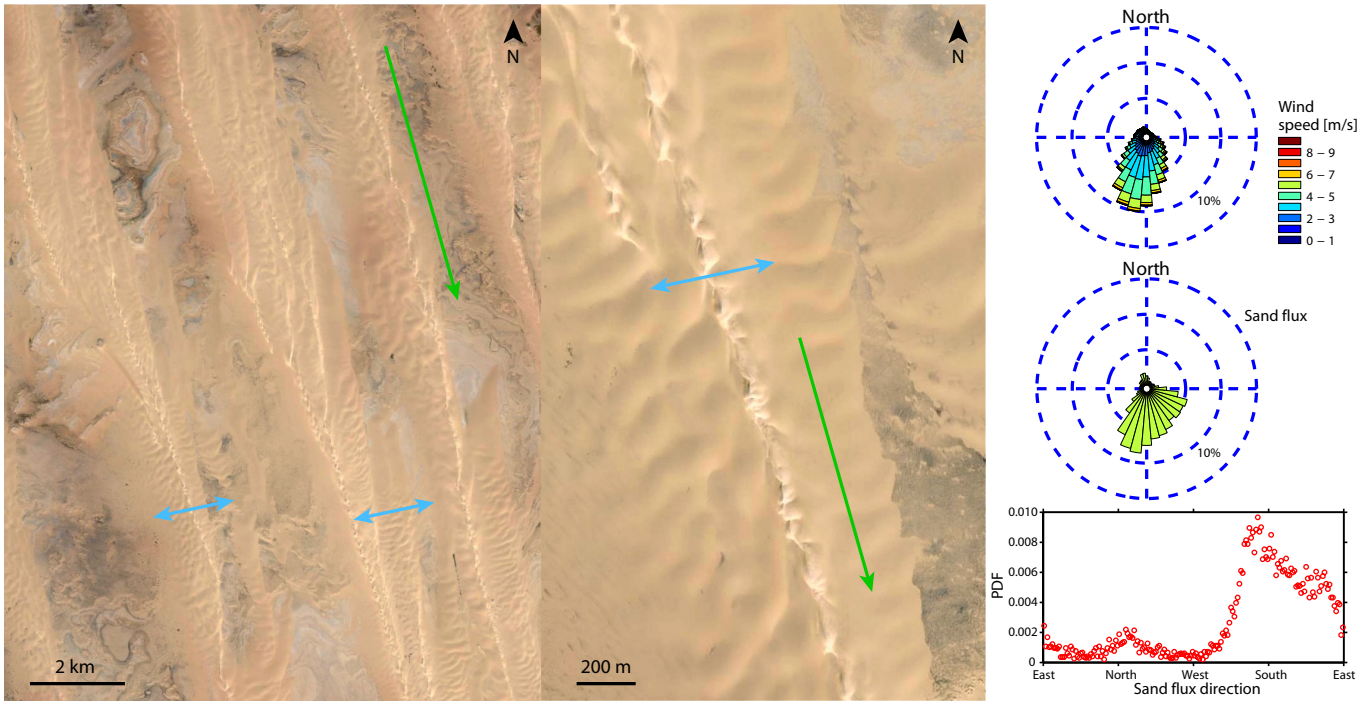

FIG. 20: Great Sand Sea (Egypt) views at different scales and corresponding sediment transport properties. Images come from Google Earth (26.03° N, 26.92° E). Coordinates of the wind rose are 26.25° N, 27° E. RDP/DP $= 0.53 \pm 0.02$ and the divergence angle of flux is 135°. Blue arrow shows the predicted orientation of the bed instability mode (12°). Green arrow shows the predicted orientation of the fingering mode (285.9°). Measured orientations are $14.3° \pm 5.4°$ for the bed instability and $285.9° \pm 4°$ for the fingering.

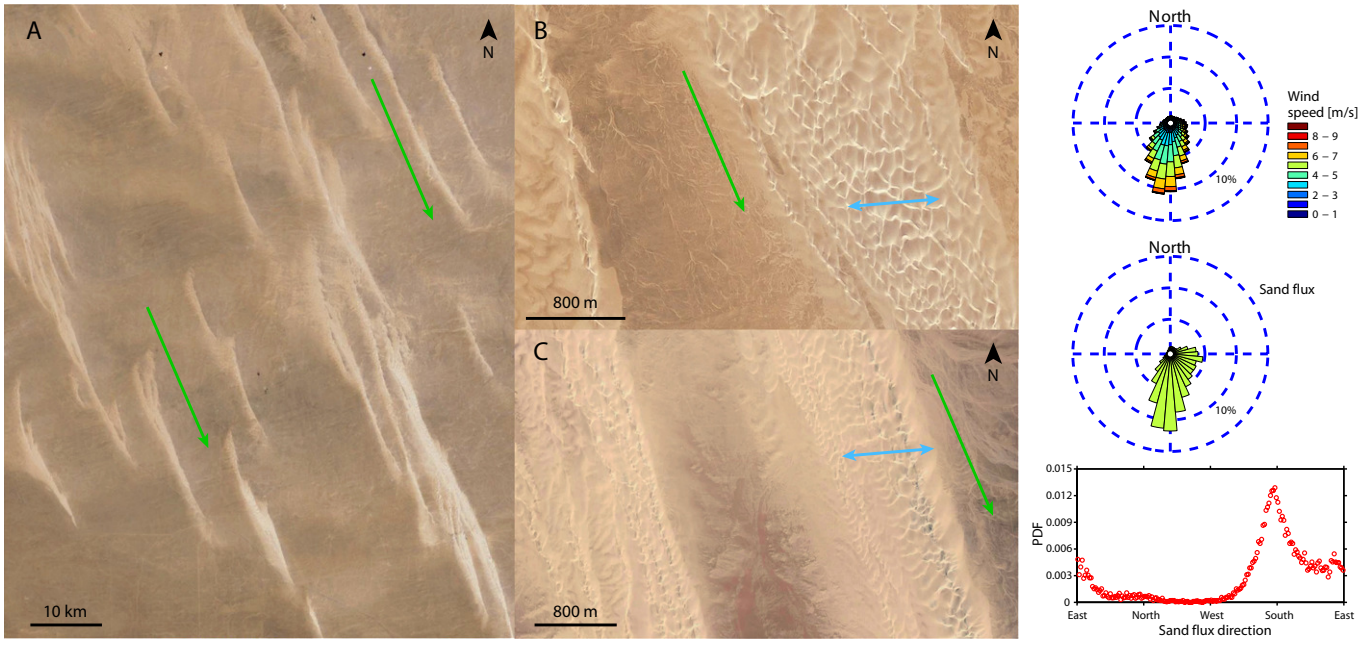

FIG. 21: North of Abu Moharik (Egypt) views at different scales and corresponding sediment transport properties. Images come from Google Earth (A: 29.66° N, 29.03° E, B: 29.61° N, 29.28° E, C: 29.39° N, 29.40° E). Coordinates of the wind rose are 29.25° N, 29.25° E. RDP/DP $= 0.65 \pm 0.01$ and the divergence angle of flux is 112°. Blue arrow shows the predicted orientation of the bed instability mode (4.8°). Green arrow shows the predicted orientation of the fingering mode (293.4°). Measured orientations are $-0.1° \pm 8°$ for the bed instability, $294.2° \pm 7°$ for the fingering at small scale and $290.7° \pm 4°$ for the fingering at large scale.

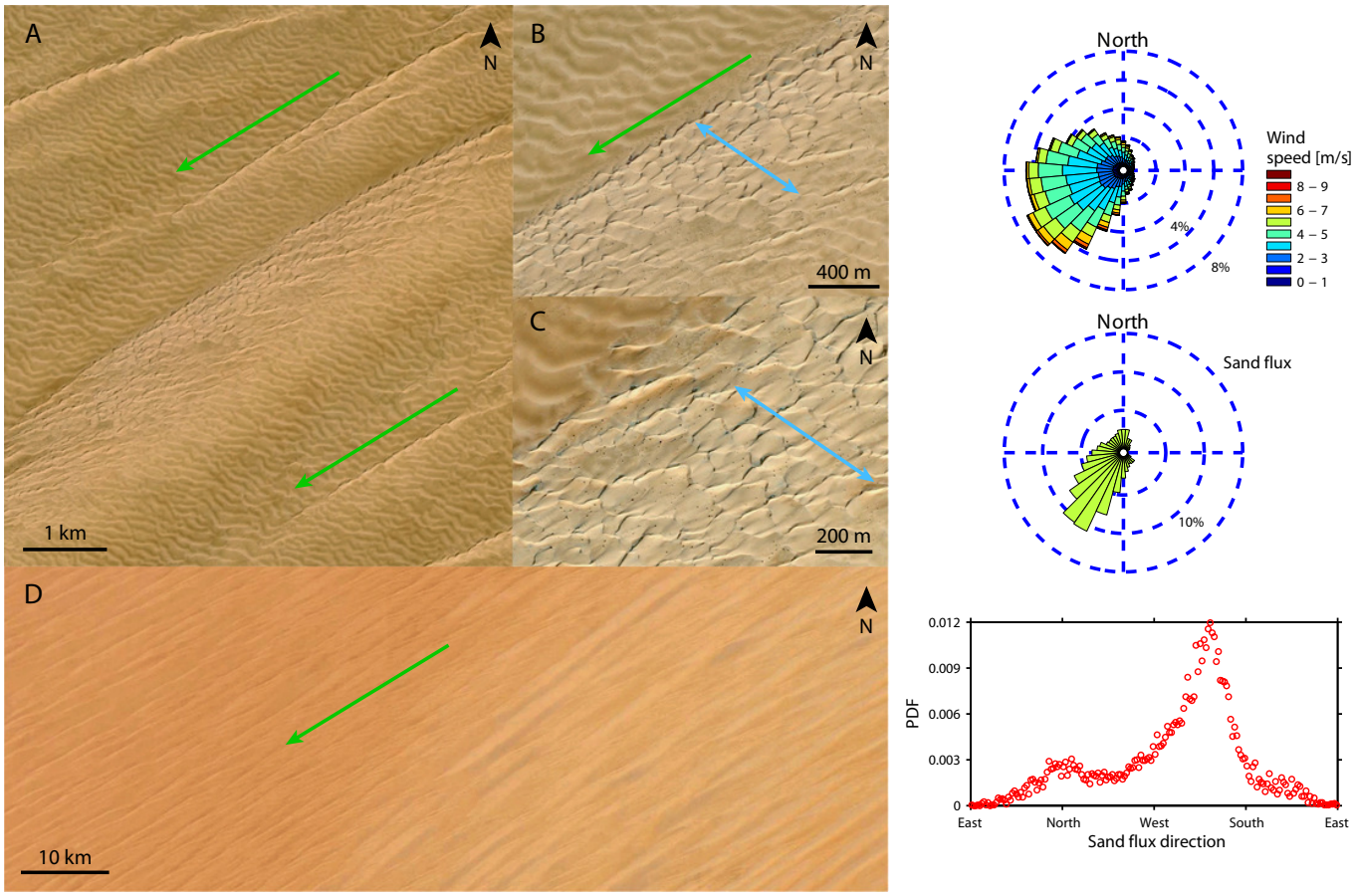

FIG. 22: Rub' al Khali desert (Saudi Arabia) views at different scales and corresponding sediment transport properties. Images come from Google Earth (A, B: 19.79° N, 47.95° E, C: 19.59° N, 47.96° E, D: 19.5° N, 48° E). Coordinates of the wind rose are 19.5° N, 48° E. RDP/DP = 0.52 ± 0.04 and the divergence angle of flux is 133°. Blue arrow shows the predicted orientation of the bed instability mode (145.6°). Green arrow shows the predicted orientation of the fingering mode (211.4°). Measured orientations are $156.3° \pm 4°$ for the bed instability, $205.9° \pm 5°$ for the fingering at small scale and $214.7° \pm 1.5°$ for the fingering at large scale. The low-contrast bedforms seen in the inter-dune areas appear to be sand sheets of segregated coarse grains [30, 51, 52].

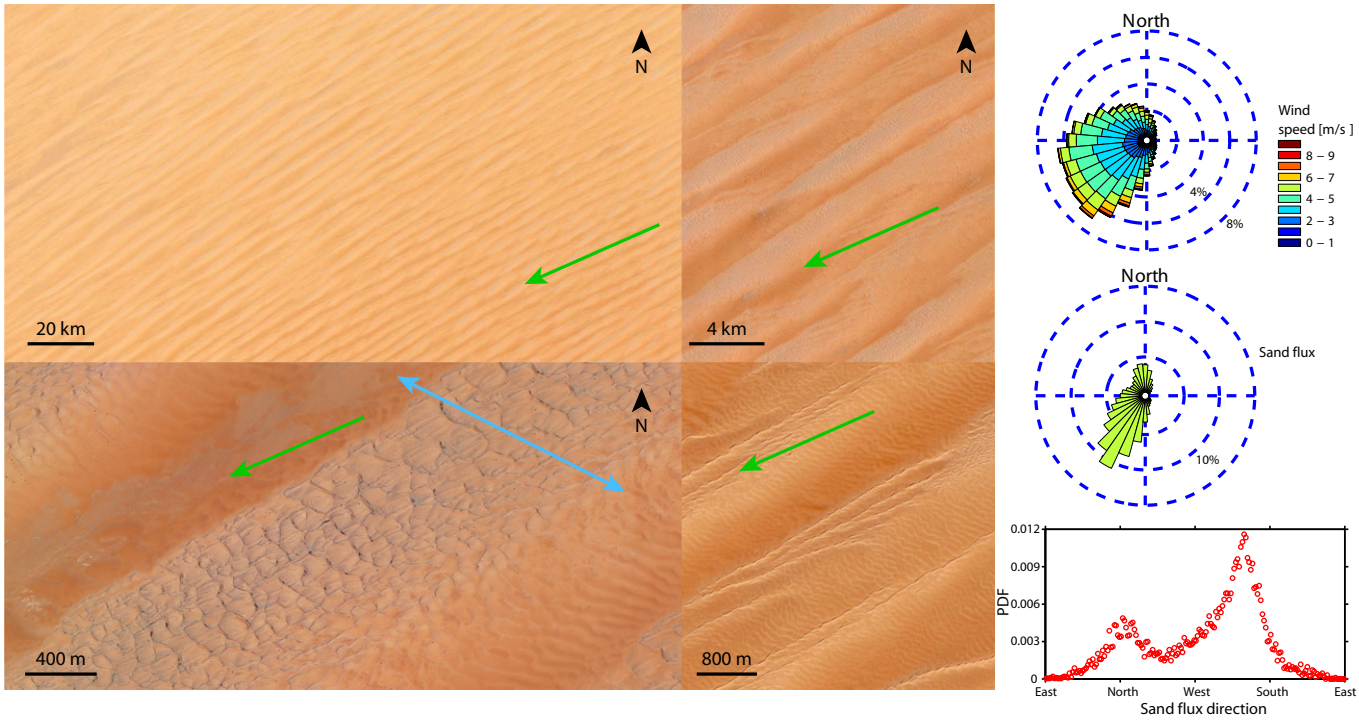

FIG. 23: Rub' al Khali desert (Saudi Arabia) views at different scales and corresponding sediment transport properties. Images come from Google Earth (19.3° N, 48.53° E). Coordinates of the wind rose are 19.5° N, 48.75° E. RDP/DP $= 0.46 \pm 0.04$ and the divergence angle of flux is 139°. Blue arrow shows the predicted orientation of the bed instability mode (153.2°). Green arrow shows the predicted orientation of the fingering mode (203.8°). Measured orientations are $140° \pm 7°$ for the bed instability, $202.6° \pm 5°$ for the fingering at small scale and $210.1° \pm 1°$ for the fingering at large scale. The low-contrast bedforms seen in the inter-dune areas appear to be sand sheets of segregated coarse grains [30, 51, 52].

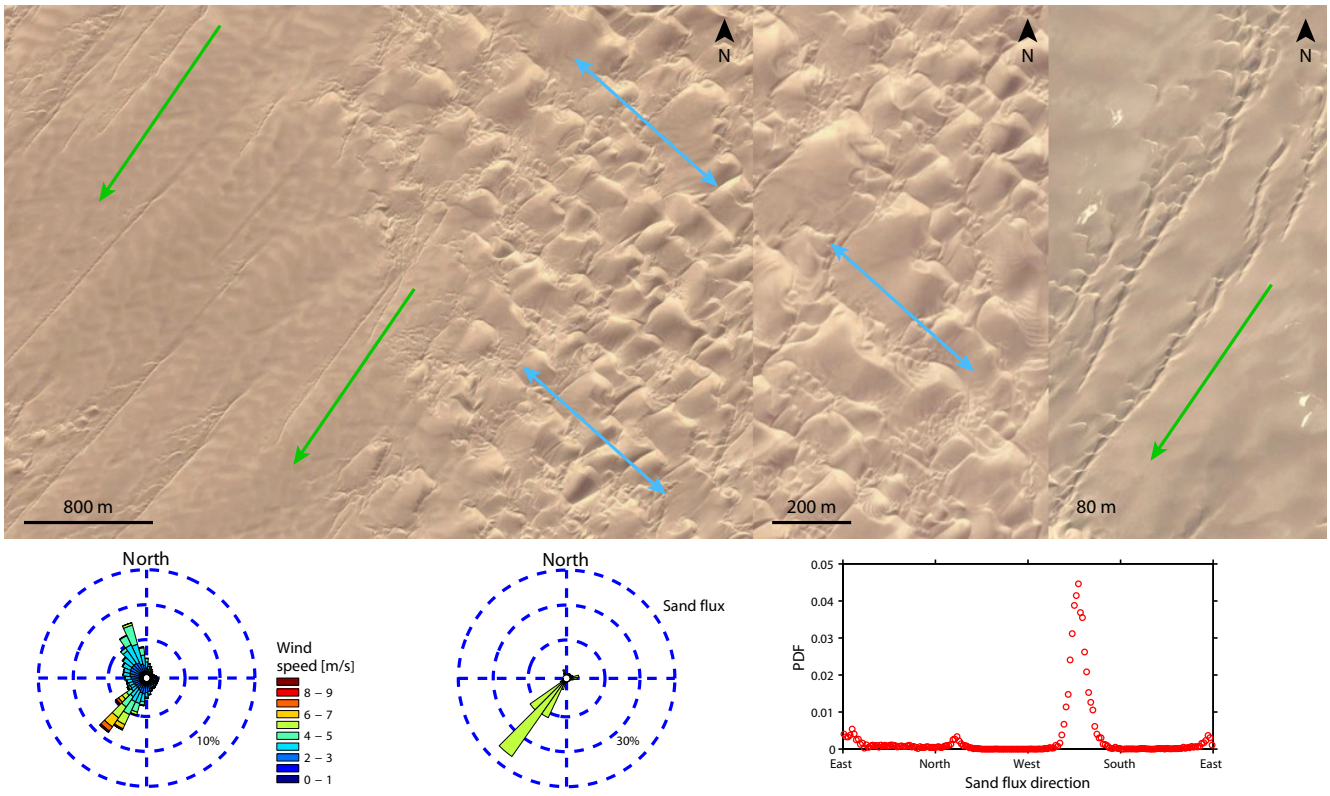

FIG. 24: South Taklamakan views at different scales and corresponding sediment transport properties. Images come from Google Earth (38.31° N, 86.31° E). Coordinates of the wind rose are 38.25° N, 86.25° E. RDP/DP = 0.62 ± 0.05 and the divergence angle of flux is 125°. Blue arrow shows the predicted orientation of the bed instability mode (138.2°). Green arrow shows the predicted orientation of the fingering mode (235.5°). Measured orientation sare $138.2° \pm 2.8°$ for the bed instability and $232° \pm 2.9°$ for the fingering. The low-contrast bedforms seen in the inter-dune areas appear to be sand sheets of segregated coarse grains [30, 51, 52].

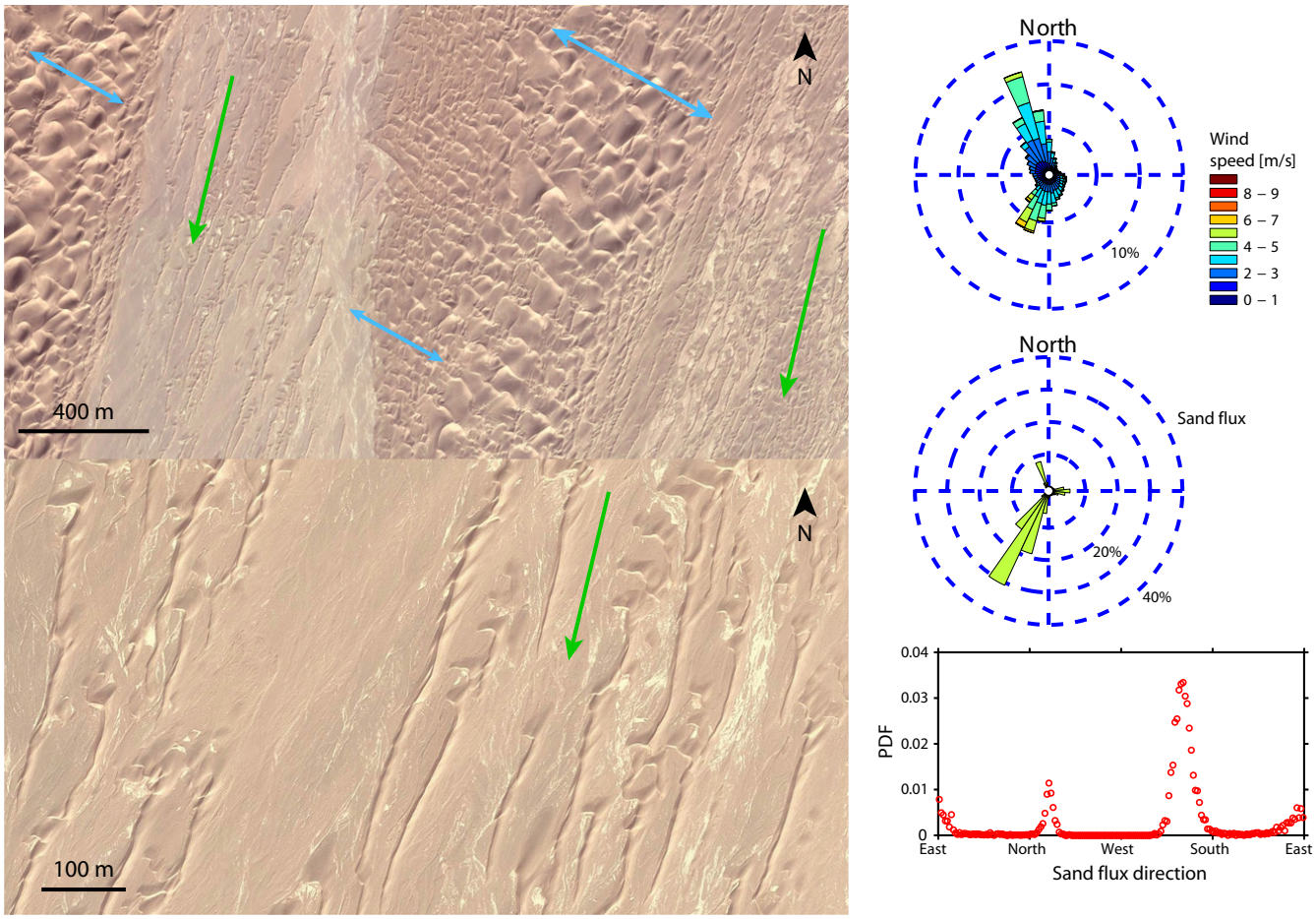

FIG. 25: South Taklamakan views at different scales and corresponding sediment transport properties. Images come from Google Earth (38.32° N, 86.67° E). Coordinates of the wind rose are 38.25° N, 87° E. RDP/DP = 0.52 ± 0.05 and the divergence angle of flux is 134°. Blue arrow shows the predicted orientation of the bed instability mode (150.9°). Green arrow shows the predicted orientation of the fingering mode (256.6°). Measured orientations are $142.6° \pm 7°$ for the bed instability and $250.8° \pm 3°$ for the fingering.

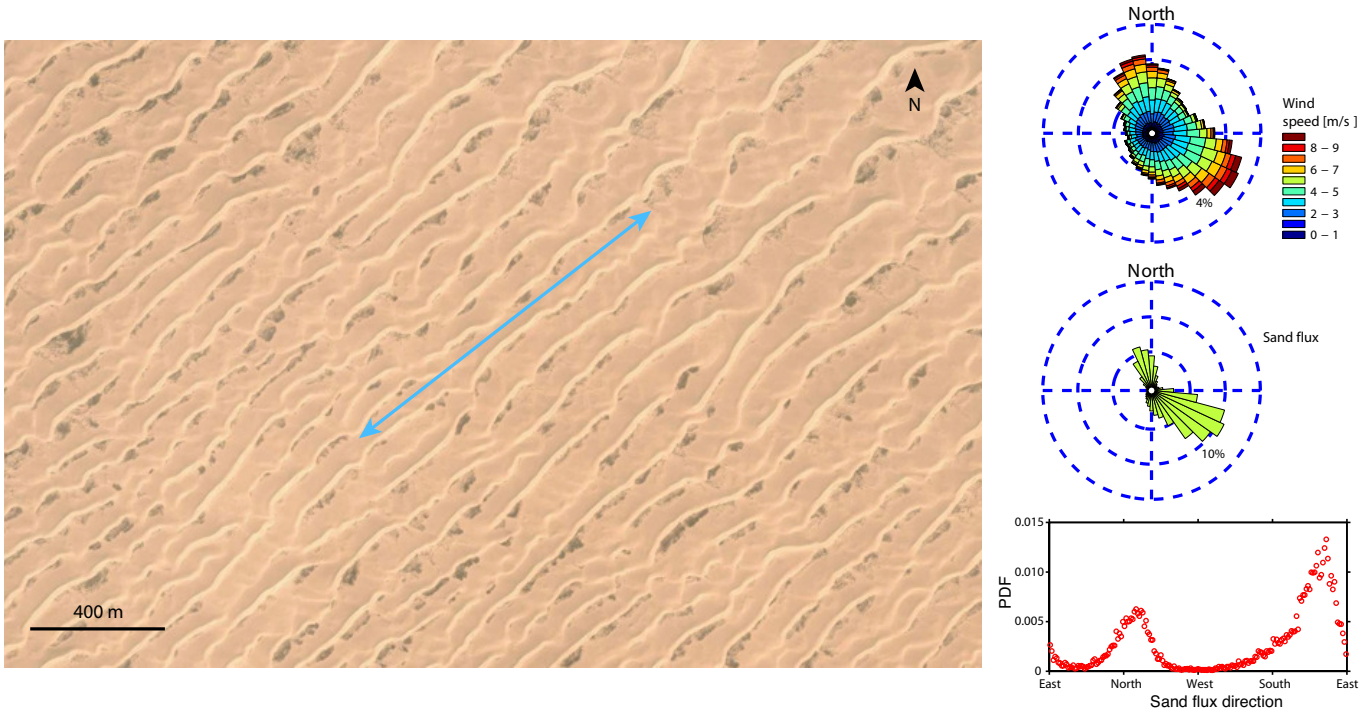

FIG. 26: Mu Us view and corresponding sediment transport properties. Image comes from Google Earth (38.83° N, 107.68° E). Coordinates of the wind rose are 39° N, 108° E. RDP/DP $= 0.44 \pm 0.04$ and the divergence angle of flux is 152°. Blue arrow shows the predicted orientation of the bed instability mode (37.9°). The measured orientation of the bed instability mode is $38.5° \pm 4.2°$.

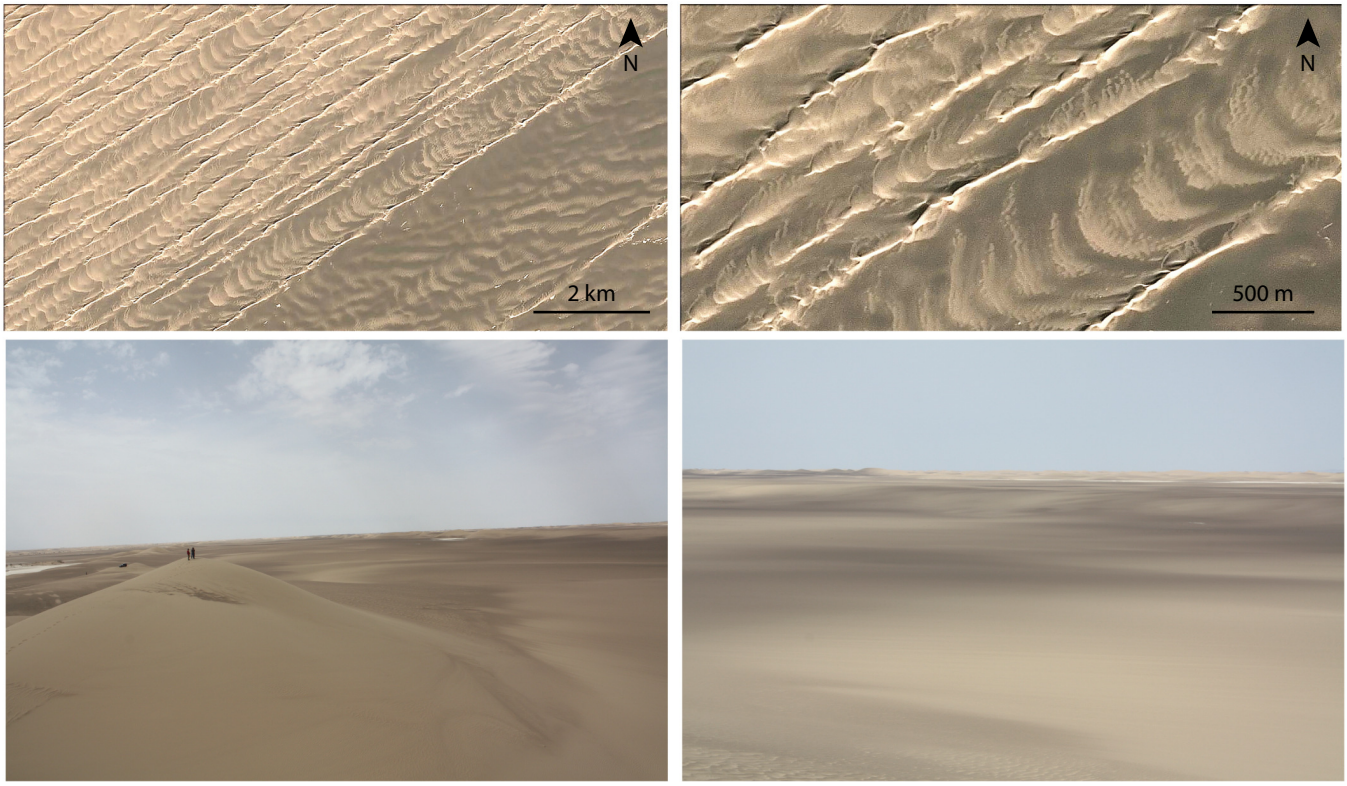

FIG. 27: Satellite and ground views of a dune field in the Kumtagh desert (China). Satellite images come from Google Earth (40.33° N, 92.61° E), C. Narteau took the ground pictures. The low-contrast bedforms that are transverse to the linear dunes are not dunes but low relief sand sheets as described in [30, 51, 52]. Coarse grains pave the ground, which makes it non-erodible.

MovieDR1-LimitedBedDunes.mp4

MovieDR2-FedBedDunes.mp4

MovieDR3-FingerDune.mp4